PCCP

S−H Rotamerization *via* Tunneling in a Thiol Form of Thioacetamide

Journal:	*Physical Chemistry Chemical Physics*
Manuscript ID	CP-ART-06-2019-003417
Article Type:	Paper
Date Submitted by the Author:	17-Jun-2019
Complete List of Authors:	Gobi, Sandor; University of Coimbra, Department of Chemistry Manaia Nunes, Cláudio ; University of Coimbra, Department of Chemistry Reva, Igor; University of Coimbra, Department of Chemistry; Tarczay, Gyorgy; Eotvos University, General and Inorganic Chemistry Fausto, Rui; University of Coimbra, Department of Chemistry
Note: The following files were submitted by the author for peer review, but cannot be converted to PDF. You must view these files (e.g. movies) online.	
Energiesvs2.emf	

SCHOLARONE™
Manuscripts

Article type: Full paper

PCCP

Physical Chemistry Chemical Physics

ROYAL SOCIETY OF CHEMISTRY

Website www.rsc.org/pccp
Impact factor* 3.906

Journal expectations To be suitable for publication in *Physical Chemistry Chemical Physics* (*PCCP*) articles must include significant new innovation and/or insight into physical chemistry.

Article type: Full paper Original scientific work that has not been published previously. Full papers do not have a page limit and should be appropriate in length for scientific content.

Authors should include a brief discussion in the Introduction that sets the context for the new work and gives their motivation for carrying out the study.

Journal scope Visit the *PCCP* website for additional details of the journal scope and expectations.

The journal has a broad scope which includes spectroscopy, dynamics, kinetics, statistical mechanics, thermodynamics, electrochemistry, catalysis, surface science, quantum mechanics and theoretical developments. Interdisciplinary research areas such as polymers and soft matter, materials, nanoscience, energy, surfaces/interfaces, and biophysical chemistry are welcomed if they demonstrate significant new innovation and/or insight into physical chemistry.

Reviewer responsibilities Visit the Reviewer responsibilities website for additional details of the reviewing policy and procedure for Royal of Society of Chemistry journals.

When preparing your report, please:
- Focus on the originality, importance, impact and reliability of the science. English language and grammatical errors do not need to be discussed in detail, except where it impedes scientific understanding.
- Use the journal scope and expectations to assess the manuscript's suitability for publication in *PCCP.*
- State clearly whether you think the article should be accepted or rejected and include details of how the science presented in the article corresponds to publication criteria.
- Inform the Editor if there is a conflict of interest, a significant part of the work you cannot review with confidence or if parts of the work have previously been published.

Thank you for evaluating this manuscript, your advice as a reviewer for *PCCP* is greatly appreciated.

<div style="text-align:center">

Dr Anna Simpson Executive Editor
Royal Society of Chemistry, UK

Professor David Rueda Editorial Board Chair
Imperial College London, UK

</div>

S–H Rotamerization *via* Tunneling in a Thiol Form of Thioacetamide

Sándor Góbi[a,*], Cláudio M. Nunes[a], Igor Reva[a], György Tarczay[b,c], and Rui Fausto[a]

[a] *CQC, Department of Chemistry, University of Coimbra, 3004–535, Coimbra, Portugal*

[b] *Laboratory of Molecular Spectroscopy, Institute of Chemistry, ELTE Eötvös Loránd University, H–1518 Budapest, Hungary*

[c] *MTA-ELTE Lendület Laboratory Astrochemistry Research Group, Institute of Chemistry, Eötvös Loránd University, H–1518 Budapest, Hungary*

*Corresponding author: sgobi@qui.uc.pt

Abstract

Rotamerization of a hydroxyl (O−H) group by tunneling is well-known and has been extensively studied. On the other hand, similar tunneling processes for the thiol (S−H) group have not been reported yet. In this work, the imino-thiol forms of thioacetamide were studied in cryogenic matrices (Ar, Xe) after UV-irradiation of the common amino-thione form of the compound. Four different imino-thiol forms were generated, corresponding to the *cis* or *trans* thiol (**C**/**T**) conformers of the two imino isomers (*syn* and *anti*; **s**/**a**). Noteworthy, the *syn-cis* (**sC**) imino-thiol form was found to convert spontaneously to the *syn-trans* (**sT**) form (with a half-life of 80 min), in a process whose reaction rate is independent of the temperature (i.e., at 11 or 20 K). Such conformational transformation represents the first experimental observation of an S−H rotamerization occurring by tunneling. Computations based on the Wentzel–Kramers–Brillouin formalism predict an S−H tunneling for the *syn*-imino **sC**→**sT** rotamerization on the time scale of minutes, in agreement with the experimental observations.

1. Introduction

Thione–thiol tautomerization has been an intriguing and widely investigated topic. In most of the compounds only the thione tautomer is populated and can be detected under standard experimental conditions in the gas phase or isolated in rare-gas matrices. However, upon UV irradiation, the thione compounds can be converted to their thiol tautomers, which can be captured and stabilized in inert matrices at low temperatures. Such molecules include 2(1*H*)-pyridinethione,[1] 4(3*H*)-pyrimidinethione and 3(2*H*)-pyridazinethione,[2] 2(1*H*)-quinolinethione,[3] methimazole,[4] 2-thiobenzimidazole,[5] thiourea,[6,7] and thioacetamide.[8] One notable exception is thiophenol, existing as thiol tautomer only.[9] Compounds with two thio groups usually have either dithione or thione–thiol as the most abundant tautomeric form, and can be successfully converted to dithiols;[10–14] furthermore, the photoreversibility of the tautomerization has also been demonstrated.[11]

The role of tunneling in molecular conformational isomerizations has been investigated in cryogenic matrices on numerous occasions.[15] Most of the reported cases involve the rotamerization of the O–H moiety of carboxylic acids isolated in different cryogenic matrices,[16–18] and include investigations on formic acid monomer and dimers,[19–22] acetic acid,[23,24] trifluoroacetic acid,[25] tribromoacetic acid,[26] propionic acid,[27] 2-chloropropionic acid,[28] propiolic acid,[29] several *α*-ketocarboxylic acids including pyruvic acid,[30,31] 2-furoic acid,[32] and 2-chlorobenzoic acid.[33] Examples of tunneling in the rotamerization of the O–H group in derivatives of carbonic acid,[34,35] amino acids,[36,37] and the nucleobase cytosine in cryogenic matrices have also been discussed in the literature.[38,39]

There are far fewer known systems that exhibit intramolecular hydrogen tunneling involving bond-breaking and making. Besides *α*-hydroxy carbonyls (such as tropolone) and the cyclic dimers of carboxylic acids being the most widely known examples,[40–42] only a handful of such processes have been reported for (hydroxy)carbenes,[43–52] ketenes,[53] nitrenes,[54] selones (selenourea),[55] as well as thiones such as thiourea and dithiooxamide[6,7,14] isolated in cryogenic matrices. Tunneling observed in the tautomerization of seleno and thio compounds follows similar trends, which are the prototropic isomerizations opposite to those induced by UV-irradiation: the photogenerated selenols and thiols convert back to selone and thione forms, respectively.

Due to the well-known occurrence of tunneling in the rotamerization of O–H groups and also in the tautomerization of hydroxyl compounds as well as seleno- and thio-derivatives, the existence of tunneling in the rotamerization of an S–H (or Se–H) group could be envisaged.[56] However, to the best of our knowledge, evidence of such tunneling processes has never been reported so far.[57] Here, we demonstrate that S−H rotamerization in a thiol form of thioacetamide captured in cryogenic matrices takes place spontaneously by tunneling. This observation proves, for the first time, that tunneling plays a role not only in conformational isomerization of oxygen-containing compounds but is also possible for their sulfur counterparts and could occur more generally than it has been considered.

2. Experimental and Computational Methods

2.1 Matrix-isolation infrared spectroscopy

The experiments reported in this work were carried out in two laboratories, in Coimbra (Portugal) and in Budapest (Hungary).

In Coimbra, a commercial sample of thioacetamide obtained from Merck (99%) was used. The sample was stored in a glass tube with a Young valve, connected to the vacuum chamber of a cryostat through a stainless steel needle valve. Before the experiments, the sample was pumped through the vacuum chamber at room temperature in order to eliminate air and other volatile impurities. Then, a CsI window used as optical substrate was cooled down to 16 K using a closed-cycle helium refrigerator with a DE-202 expander (Advanced Research Systems) with a base pressure of approximately 10^{-7} mbar. The sample vapor was co-deposited with an excess of Ar (Air Liquide, purity 99.9999%) or Xe (Linde, 99.999%) onto the optical substrate. After the deposition, the temperature of the sample was lowered to 11 K. The temperature of the cold window was measured directly by a silicon diode sensor connected to a LakeShore 331 digital temperature controller, which also allows for the stabilization of the sample temperature with an accuracy of 0.1 K. The sample sublimation temperature was kept at 320 K to achieve the desired vapor pressure and therefore deposition rate. During and after the deposition, mid-IR spectra of the growing or deposited sample were collected (128 scans) using a Nicolet 6700 FT-IR spectrometer equipped with a deuterated triglycine sulfate (DTGS) detector and a Ge/KBr beamsplitter (experiment **1**). The FT-IR spectra were also taken using a

2

mercury cadmium telluride (MCT) detector cooled with liquid nitrogen (experiments **2** and **3**). The same spectral collection parameters (4000–400 cm^{-1} region, 128 scans, and 0.5 cm^{-1} resolution) were used for experiments **1**, **2**, and **3**.

In Budapest, a commercial sample of thioacetamide obtained from Sigma-Aldrich (>99.0%) was used. Similarly to the experiments undertaken in Coimbra, the compound was kept in a glass tube with a Young valve, connected to the vacuum chamber of a cryostat, and, before the experiments, the sample was pumped through the vacuum chamber in order to eliminate air and other volatile impurities. The CsI optical substrate of the cryostat was cooled down to 11 K using a closed-cycle helium refrigeration system (Janis CCS-350R cold head cooled by a CTI Cryogenics 22 refrigerator) with a base pressure of approximately 10^{-6} mbar. The sample vapor was co-deposited with an excess of Ar (Messer, 99.9999%) onto the optical substrate. The temperature of the cold window was measured by a silicon diode sensor connected to a LakeShore 321 digital temperature controller. The sample sublimation temperature was 318 ± 5 K. The mid-IR spectra obtained during and after the deposition of the samples were collected (64 scans) in the 4000–400 cm^{-1} region with 1 cm^{-1} resolution using a Bruker IFS 55 FT-IR spectrometer equipped with an MCT detector cooled with liquid nitrogen and a KBr beamsplitter (experiment **4**).

2.2 Irradiation experiments

In Coimbra, the deposited matrices were irradiated through a quartz window of the cryostat. In experiments **1** and **2**, the UV irradiation of the thione precursor was done using a frequency-tunable monochromatic light provided as signal beam of an Optical Parametric Oscillator (Spectra-Physics MOPO-SL, fwhm ≈ 0.2 cm^{-1}, duration = 10 ns) pumped with a pulsed Nd:YAG laser (Spectra-Physics PRO-230, output power (P) ≈ 4.5 W, wavelength (λ) = 355 nm, repetition rate (f) = 10 Hz). A frequency-doubling unit (Spectra-Physics MOPO FDO-970) was utilized, with the wavelength of the irradiating beam set to 269.5 nm or 285 nm in experiments **1** and **2**, respectively. The overall irradiation time was 3 min (P ≈ 13 mW) in experiment **1**, and 31 min (P ≈ 10 mW) in experiment **2**. In experiment **3**, a Hg(Xe) lamp (Newport model 6697; output power: 250 W), coupled to a water filter, was used as UV source, with the irradiation time being 60 min. All the above irradiation wavelengths fall within the first UV-absorption band of thioacetamide, with an onset near 300 nm and a maximum near 266 nm.[58]

In the Budapest experiment (**4**), the deposited matrices were irradiated *in situ* through the outer KBr window of the cryostat applying a frequency-tunable monochromatic light provided as signal beam of an Optical Parametric Oscillator (OPO; GWU/Spectra-Physics VersaScan MB 240, fwhm $\approx$ 5 cm^{-1}) pumped by a pulsed Nd:YAG laser (Spectra-Physics Quanta Ray Lab 150, $P \approx$ 2.1–2.2 W, λ = 355 nm, f = 10 Hz, duration = 2–3 ns). The OPO beam was perpendicular to the FT-IR spectrometer beam. The CsI cold window was rotated 45° relatively to both the FT-IR and the OPO beams. The wavelength of the irradiating beam was set to 275 nm, with the overall irradiation time being 60 min ($P \approx$ 25 mW).

2.3 Kinetic studies

In experiment **1**, the thione→thiol conversion was achieved by means of UV-irradiation, in a similar way as reported in Ref. 8. After that, the kinetics of the spontaneous decay of the thiol isomers was monitored. These decays were monitored in independent experiments at 11 K (experiment **1a**) and 20 K (experiment **1b**). In order to protect the sample against infrared irradiation with photons exceeding the energy of 10.4 kJ mol^{-1}, a Spectrogon LP11500 nm longwave-pass cut-off filter (transmitting only below 870 cm^{-1}) was placed between the spectrometer light source and the cryostat. The effect of complete blocking of the spectrometer beam source was investigated after the irradiation of the deposited sample in experiment **2**. In experiment **3**, a different matrix gas (xenon, instead of argon) was examined, to study the effect of matrix host on the spontaneous decay (at 11 K). In order to further investigate the spontaneous decay in the presence or absence of filters, the kinetic studies were repeated again, for the compound in argon matrix, without using any filter (experiment **4a**) or using a longwave-pass filter having a cut-off wavenumber of 1960 cm^{-1} (experiment **4b**).

In the Eyring–Polányi equation (see Section 3.3), k is the reaction rate (in s^{-1}), κ is the transmission coefficient usually assumed to be 1 (no tunneling), k_B the Boltzmann constant (1.38 × 10^{-23} J K^{-1}), T is the temperature (in K), h is Planck's constant (6.626 × 10^{-34} J s), R is the gas constant (8.314 J mol^{-1} K^{-1}), and $\Delta^{\ddagger}G^{\ominus}$ is the standard Gibbs free energy of activation of the studied compound.

2.4 Theoretical computations

The quantum chemical computations were performed using the Becke's three parameter hybrid functional B3LYP, with the non-local and local correlation described by the Lee–Yang–Parr and the Vosko–Wilk–Nusair III functionals, respectively,[59–61] together with the Pople-type 6-311++G(3df,3pd) basis set,[62] as implemented in Gaussian 09.[63] The isomerization barriers were investigated starting by the optimization of the transition states (TSs) using the Berny algorithm,[64] followed by the computation of the intrinsic reaction paths (IRPs) in Cartesian coordinates.[65] The tunneling rates were computed using the Wentzel−Kramers−Brillouin (WKB) model, described in detail elsewhere.[66] In the equation used to predict the tunneling probabilities ($P(E)$) in Section 3.4, m is the particle mass (1.68×10^{-27} kg for H), (V_0–E) is the difference in energy of the particle (E) with respect to the barrier height (V_0, both in J), h is Planck's constant and w is the width of the barrier (in m) at the particle energy E. By multiplying $P(E)$ with the frequency of attempts (v, in s^{-1}) estimated by the frequency of the vibrational mode participating in the process ($\tilde{v}$, in m^{-1}) one obtains the tunneling rate (k, in s^{-1}), which can be converted to the half-life ($t_{1/2}$ = ln2 / k, in s^{-1}). Note that $\tilde{v} = v/c$, where c is the speed of light and equals 299 792 458 m s^{-1}. The energies of the thioacetamide conformers and those of the TSs were also obtained from the structures optimized with the complete basis set (CBS-QB3)[67] and Gaussian-4 (G4)[68,69] methods, which are well-known to allow for very accurate determination of energies.

3. Results and Discussion

3.1 Computations on the Thioacetamide Isomeric Forms

Figure 1 presents the structures of thione and thiol isomeric forms of thioacetamide as optimized at the B3LYP/6-311++G(3df,3pd) level of theory. The structures of the TSs between these forms were also optimized and are shown in Figure 2. Table 1 summarizes the energetics of all the structures (the geometries, energies, and harmonic vibrational frequencies are shown in Tables S1–S31; Supporting Information). Overall, the results support the previous theoretical findings.[58,70]

According to the computed energies of the different thioacetamide isomeric forms, it is expected that it adopts exclusively the amino-thione form (hereafter denoted as **Tn**) in the sample after deposition, since this form is stabilized by more than 38 kJ mol^{-1}

5

comparing to the imino-thiol forms. The imino-thiol forms can have two orientations of the N−H group (denoted as *anti* (**a**) and *syn* (**s**), differing in their dihedral angle H−N=C−S, φ_1), as well as two orientations of the S−H group (denoted as *trans* (**T**) and *cis* (**C**), differing in their torsional angle H−S−C=N, φ_2). For the definition of φ_1 and φ_2 and their values please refer to Figure 1 and Table 1. All possible combinations of **a/s** and **T/C** orientations result in four different thiol isomers. Based on the computational results *syn* (**s**) imino forms are relatively more stable than the *anti* (**a**) forms (stability order: **sT** > **sC** > **aC** > **aT**). Furthermore, five different TS structures were considered, one accounting for the **Tn** to thiol conversion (**Tn–aC**, Table 1), whereas the others interconnect the *anti* and *syn* imino isomers in keeping the conformation of the thiol group (**aC–sC** and **aT–sT**), or the *trans* and *cis* thiol conformers of each imino isomer (**aC–aT**, **sC–sT**). It should be noted that both the **aC–aT** and **sC–sT** TSs exist in pairs, as mirror-images of each other (1 and 2) and therefore have identical energies. An interesting structural feature is the fact that the orientation of the methyl group is different in thione compared to the thiol tautomer and the TSs, with one methyl hydrogen atom eclipsing the sulphur atom in the former, whereas eclipsing the nitrogen atom in the latter.

In order to obtain the relative energies, especially for the *cis* (**C**) and *trans* (**T**) thiol forms, the use of the B3LYP/6-311++G(3df,3pd) level of theory was necessary. Compounds containing sulfur atoms notoriously require the extensive use of polarization and diffuse functions in order to accurately predict their energies; it has been shown that this applies not only to hypervalent but to divalent sulfur atoms as well.[71,72] Computations applying the CBS-QB3 and G4 methods, known for the reliable prediction of the relative energies and barrier heights,[73,74,75] were then also performed in the present study (Tables S32–S57). The obtained results were found to agree with the energies of the thioacetamide isomeric forms computed at the B3LYP/6-311++G(3df,3pd) level of theory. Therefore, computations at the B3LYP/6-311++G(3df,3pd) level of theory were also used to characterize the intrinsic reaction paths (IRC computations) that were used in this work to estimate the tunneling probabilities (Section 3.4).

3.2 Thioacetamide Thiol Forms Generated and Captured in Cryogenic Matrices

The IR spectra obtained after matrix deposition indicate the sole presence of the thione (**Tn**) monomeric form in the as-deposited matrices (Figure S1a). Upon the performed UV irradiations, **Tn** gradually converts into the four thiol isomers (Figure S1b). This

observation generally agrees with the results described before by Lapinski et al.[8] Interestingly, in the case of the oxo-counterpart of the studied compound, i.e., acetamide, only two *syn*-imino-enol isomers exist in the matrix after irradiation.[76] After generating the thiol forms by UV irradiation of their thione precursor, we found that the bands due to **sC** form spontaneously decreased in intensity, while those ascribed to **sT** simultaneously increased. This observation, testifying the occurrence of a conformational change through S–H rotamerization, is shown in Figure 3b, depicting the overnight spectral changes in the 855–600 cm^{-1} region that occurred in the dark, for an argon matrix kept at 11 K. The experimentally observed UV-induced and subsequent spontaneous (with or without filter, as will be discussed further) IR spectral changes (Table 2), supported by the comparison between the experimental and the simulated IR spectra allowed for the unambiguous assignment of all four photogenerated thiol forms in the above-mentioned region of the IR spectrum (Figure 3).

3.3. Kinetics of the Observed S-H Rotamerization

It is always tempting to assume that at cryogenic temperatures (of a few K, as in the present experiments) spontaneous changes in the IR spectra are due to tunneling. Nonetheless, to unequivocally establish the occurrence of such a process, the possibility of other contributions has to be considered. In particular, the effect of the IR globar source of the spectrometer and the thermal energy may induce conformational isomerization processes in matrix-isolated samples.[38,39,77] Accordingly, the broadband IR beam of the spectrometer either needs to be completely blocked between the measurements or the photons energetic enough to induce changes in the sample have to be filtered. Moreover, thermal effects need to be completely ruled out. Therefore, in order to separate different factors that may affect the spontaneous decay rate of thioacetamide thiol forms (temperature, effect of the spectrometer source, and also the effect of the matrix host), we conducted a series of dedicated experiments under different conditions: (i) spectra were recorded using a longpass filter with a cut-off wavenumber of 870 cm^{-1} (experiment **1** as described in Section 2) at two different temperatures (experiments **1a** and **1b**); (ii) the spectrometer beam was blocked overnight, therefore keeping the sample in complete dark (experiment **2**); (iii) the compound was isolated in a different host matrix (Xe, experiment **3**); (iv) no filter (experiment **4a**), or a longpass filter with the cut-off wavenumber of 1960 cm^{-1} (experiment **4b**) were used during recording of spectra. Note that the filter cut-off

at 870 cm^{-1} (10.4 kJ mol^{-1}) is significantly lower than the computed barrier for the **sC** to **sT** rotamerization (16.4 kJ mol^{-1}) and other isomerizations (Table 1). Thus, with this filter, the impending photons of the filtered beam should not have enough energy to induce any over-the-barrier isomerization. With the cut-off value set at the higher value of 1960 cm^{-1} (23.4 kJ mol^{-1}), the impending photons have enough energy to induce over-the-barrier **sC** → **sT**, **sT** → **sC**, and **aT** → **aC** rotamerizations. Without filter, all the **C** → **T** or **T** → **C** over-the-barrier rotamerizations of the S–H group may be stimulated by the infrared light.

In experiment **4a** (sample exposed to the IR light from the globar without filter), intensity changes could be observed for bands ascribed to all four thiol conformers. Some of these changes must be caused by the photons originating from the spectrometer source (Figure S2). Furthermore, the final **sC** : **sT** population ratio is significantly higher in experiment **4a** (**sC**$_f$: **sT**$_f$ ≈ 0.2, Table 3) than in experiments **1a**, **1b**, and **4b** (**sC**$_f$: **sT**$_f$ ≈ 0.1, Table 3). This implies that the unfiltered radiation from the spectrometer source leads to a different stationary state compared to the measurements conducted with filters. This also applies to the experiment during which the IR globar source was completely blocked (experiment **2**) and the sample was kept in dark, thus excluding the effect of broadband IR irradiation and thermal effects.

Figure 4 shows the kinetic decay/growth curves of conformers **sC** and **sT** during experiment **1a**, whereas Figures S3–S7 allow to visualize the same for experiments **1a** (extended version), **1b**, **3**, **4a**, and **4b**, respectively. For fitting the decay curves, a single exponential decay function was used:

$$A_t(sX,\nu_y) = A_{t\,=\,0}(sX,\nu_y)e^{-kt} + A_{t\,=\,\infty}(sX,\nu_y) \tag{1}$$

$$t_{1/2} = \frac{ln2}{k} \tag{2}$$

where $A_t(\nu X)$ is the integrated area (in cm^{-1}) of the band ν_y of conformer sX (X = **C** or **T**; y = 623 or 836 cm^{-1} if X = **C** and y = 626 or 849 cm^{-1} if X = **T**), t is time (in min), k is the first-order rate constant (in min^{-1}), $t_{1/2}$ is the half-life (in min). The following equation was used to fit the growth curves:

$$A_t(sX,\nu_y) = A_{t\,=\,\infty}(sX,\nu_y)(1 - e^{-kt}) \tag{3}$$

8

Table 3 summarizes the decay/growth rates determined by using the functions described in equations (1) and (3). The **sC** and **sT** decay/growth rates do not significantly differ from each other at 11 and 20 K suggesting a non-Arrhenius behavior and, therefore, the occurrence of tunneling. Indeed, using the Eyring–Polányi equation (classical rate model assuming exclusively the thermal over-the-barrier reaction),

$$k = \frac{\kappa k_{\mathrm{B}} T}{h} e^{-\frac{\Delta^{\ddagger} G^{\ominus}}{RT}} \tag{4}$$

the half-life of the **sC** $\rightarrow$ **sT** reaction is calculated to be some 10^{27} years at 11 K (c.f. the measured value of 80 minutes, Table 3, $\Delta^{\ddagger}G^{\ominus} = 18$ kJ mol^{-1} was extracted from the theoretical harmonic vibrational computations).

It should be emphasized that **sC** has a nonzero abundance after 18 hours of the monitoring of its decay, which cannot be caused by the excitation of the source beam, since this can be observed in each case even if filters are used. The residual integrated band area for the band at 836 cm^{-1} is roughly 0.005 ± 0.001 cm^{-1} in the cases when filters were used and approximately twice as large (0.010 ± 0.001 cm^{-1}) in the absence of a filter (experiment **4a**). The non-zero final concentration of the higher-energy form in tunneling processes is not unusual. It may indicate the existence of a matrix site where tunneling does not occur, or occurs extremely slowly, which could explain the nonzero integrated areas after tens of hours of kinetic monitoring (18 hours in this work). Indeed, Schreiner and co-authors studied tunneling in oxalic acid and "*developed a general kinetic model to explain the temporal evolution of numerous experimental infrared bands as a tool to deconvolute the experimental spectra acquired over long time periods (up to 19 days).*"[78] Their phenomenological model was based on only two classes of matrix sites, "fast" and "slow". The "fast" tunneling half-lives (30–43 hours) were in an excellent agreement with those determined from high-level quantum chemical computations in the gas phase. However, the "slow" half-lives, differing from "fast" kinetics by an order of magnitude (260–355 hours),[78] were also detected implying that tunneling sensitively depends on the environment. Earlier, some of the present authors studied tunneling in matrix-isolated squaric acid, and also observed "fast" and "slow" tunneling decays, with respective half-lives differing by more than an order of magnitude.[79] An important observation in the study of squaric acid was that the two trapping sites characterized by "fast" and "slow" decays could be spectroscopically distinguished in some spectral ranges (band doublets with spectrally different maxima), while some other vibrations exhibited only one

9

maximum with the "fast" and "slow" sites spectrally non-distinguishable (appearing at the same peak frequency).[79] The experimental findings of the present study also point out that the **sC** imino-thiol form of thioacetamide exhibits "fast" and "slow" tunneling decay, however, the respective trapping sites cannot be spectrally distinguished for the **sC** bands appearing in the range below 840 cm^{-1} accessible for the decay monitoring.

3.4 Tunneling Computations

In order to better understand the role of tunneling in the isomerization reactions of thioacetamide, tunneling rates were theoretically estimated for multiple possible pathways. First, the TSs were identified and then the intrinsic reaction paths were obtained by running IRCs computations, thus allowing for the estimation of the width and height of the barriers. Figure 5 and Figure S8 show the IRC profiles between the thioacetamide isomers as computed at the B3LYP/6-311++G(3df,3pd) level of theory. Then, based on the WKB approximation mentioned in Section 2.4, the equation for a parabolic barrier was used to predict the tunneling rates via the computed reaction paths:

$$P(E) = e^{-\pi^2 w \sqrt{2m(V_0 - E)}/h} \tag{5}$$

Table 4 summarizes the calculated tunneling rates of the selected processes. The hydrogen tunneling for the tautomerization resulting in the formation of **Tn** from **aC** was estimated to have a $t_{1/2}$ of 100 days (Table 4). This agrees with the lack of detection of any spontaneous process yielding the **Tn** precursor.[8] The computed tunneling for the *anti→syn* imine isomerization from **aC** to **sC** has a similar $t_{1/2}$ value (100 days), whereas for the *anti→syn* imine isomerization from **aT** to **sT** the $t_{1/2}$ value was computed to be an order of magnitude faster (roughly 5 days). Taking into account the uncertainty of the computational results, the only two processes that have computed tunneling half-lives compatible with the time scale of our experiments are the *trans→cis* S−H rotamerization of the *anti*-imine (**aT** → **aC**, $t_{1/2} \approx 2.3$ h) and *cis→trans* S−H rotamerization of the *syn*-imine (**sC** → **sT**, $t_{1/2} \approx 3$ min). Moreover, both processes can take place through two symmetry-equivalent barriers (characterized by mirror-image TSs, Figure 2), and, therefore, the chance of tunneling becomes twice as high, meaning theoretical half-lives of 1.1 h and 1.5 min. However, the computed tunneling half-life values are extremely sensitive to the shape of IRC profiles, and therefore, not expected to be completely accurate. For instance, Nunes et al. showed that a slight increase of 5% in the width of a barrier (w) can cause a six-fold decrease in the calculated tunneling rates.[54] The tunneling

10

transformation with the shortest computed half-life (S−H rotamerization of **sC → sT**), i.e. with the higher tunneling probability, was the only one observed experimentally. The measured tunneling half-life time $t_{1/2}$ for the **sC → sT** process was approximately 80 minutes in argon matrices (Table 3). No other spontaneous decay was detected during the measurements.

According to the tunneling computations, the **sC → sT** process is estimated to be approximately 46 times faster than the **aC → aT** process (Table 4). Using the $t_{1/2}$ value for the **sC → sT** process obtained experimentally (80 minutes) and based on the ratio of the computed values, the **aT → aC** tunneling should take place in roughly 2.6 days. The half-life values for the other pathways are 270 days (**aT → sT**), and 15 years (**aC → sC** as well as **aC → Tn**) when applying the same calculation. Therefore, an additional but slower S−H rotamerization corresponding to the **aT → aC** conversion is still predicted to occur by tunneling within the timescale of the experiments. However, there was no discernible evidence for such a process during the performed overnight experiments (after 18 hours, approximately 18% conversion could be expected). This finding seems to contradict both what one would think intuitively (before the tunneling calculations) and the theoretical results, i.e. the occurrence of tunneling in the S−H rotamerization should be expected for both the *anti-* and *syn*-imine forms, considering the similarity of their structures, as well as the relatively close predicted values for barrier heights and widths. However, the experimental results point to a selective tunneling S–H rotamerization in the *syn*-imine form of thioacetamide. This may be either caused by different interaction of the matrices with the *anti-* and *syn*-imines, which may change the shape of the barriers or by the different energy gaps between the donor (in the reactant) and acceptor (in the product) levels, which may favor or disfavor the two processes in a considerably different way as well as by the assumptions made by the applied tunneling computational method. This also indicates that imino-thiol systems need further, more advanced, theoretical investigations to be completely understood.

4. Conclusion

Tunneling in molecular conformational isomerizations is an important topic that has been reported by dozens of works in the literature in the past few decades. With a few notable exceptions, most of these papers examine the spontaneous rotamerization

11

occurring in molecules containing O−H group(s). In contrast, although several thioxo-(and selenoxo-) compounds have been studied and provided evidence for the tautomeric thiol → thione (selenol → selone) conversions via spontaneous intramolecular hydrogen atom transfer, the *cis–trans* isomerization of S−H (Se−H) groups via tunneling has never been described before. In this work, thiol forms of thioacetamide isolated in Ar (and Xe) matrices were investigated by the help of matrix-isolation mid-IR spectroscopy, and kinetic studies were carried out at different temperatures and in the presence of various filters in order to exclude chemistry induced by the photons originating from the spectrometer light source. The measurements were accompanied by quantum chemical computations, which allowed for the estimation of the energies of the isomers as well as the TSs. IRC pathways were also computed in order to help interpret the experimental results.

Although UV irradiation produces the more energetic thiol forms, no evidence of spontaneous conversion could be found for the reverse thiol (**aC**) to thione (**Tn**), nor for between the *anti* and *syn* forms, or isomerizations between the two *anti*-imino forms (**aC** and **aT**). However, hydrogen atom tunneling takes place resulting in the selective conversion of one of the *syn*-imino thiol isomers (**sC**) to the other (**sT**). Therefore, this work shows, for the first time, that this type of spontaneous rotamerization exists not only in hydroxy compounds but also in their thiol analogs as well, which hopefully opens a new chapter in the study of hydrogen atom tunneling in molecules with thiol groups.

Acknowledgements

References

1. M. J. Nowak, L. Lapinski, H. Rostkowska, A. Leś and L. Adamowicz, *J. Phys. Chem.*, 1990, **94**, 7406–7414.

2. M. J. Nowak, L. Lapinski, J. Fulara, A. Leś and L. Adamowicz, *J. Phys. Chem.*, 1991, **95**, 2404–2411.

3. D. Prusinowska, L. Lapinski, M. J. Nowak and L. Adamowicz, *Spectrochim. Acta A*, 1995, **51**, 1809–1826.

4. E. M. Brás and R. Fausto, *J. Mol. Struct.*, 2018, **1172**, 42–54.

5. E. M. Brás and R. Fausto, *J. Photochem. Photobiol. A*, 2018, **357**, 185–192.

6. H. Rostkowska, L. Lapinski, A. Khvorostov and M. J. Nowak, *J. Phys. Chem. A*, 2003, **107**, 6373–6380.

7. H. Rostkowska, L. Lapinski and M. J. Nowak, *Phys. Chem. Chem. Phys.*, 2018, **20**, 13994–14002.

8. L. Lapinski, H. Rostkowska, A. Khvorostov and M. J. Nowak, *Phys. Chem. Chem. Phys.*, 2003, **5**, 1524–1529.

9. I. Reva, M. J. Nowak, L. Lapinski and R. Fausto, *Phys. Chem. Chem. Phys.*, 2015, **17**, 4888–4898.

10. H. Rostkowska, L. Lapinski and M. J. Nowak, *J. Phys. Org. Chem.*, 2010, **23**, 56–66.

11. H. Rostkowska, L. Lapinski, I. Reva, B. J. A. N. Almeida, M. J. Nowak and R. Fausto, *J. Phys. Chem. A*, 2011, **115**, 12142–12149.

12. L. Lapinski, M. J. Nowak, R. Kołos, J. S. Kwiatkowski and J. Leszczyński, *Spectrochim. Acta A*, 1998, **54**, 685–693.

13. H. Rostkowska, L. Lapinski and M. J. Nowak, *J. Phys. Chem. A*, 2003, **107**, 804–809.

14. L. Lapinski, H. Rostkowska, A. Khvorostov, M. Yaman, R. Fausto and M. J. Nowak, *J. Phys. Chem. A*, 2004, **108**, 5551–5558.

15. R. P. Bell, *The Tunnel Effect in Chemistry*, Chapman and Hall, New York, 1980.

16. E. M. S. Maçôas, L. Khriachtchev, M. Pettersson, J. Lundell, R. Fausto and M. Räsänen, *Vib. Spectrosc.*, 2004, **34**, 73–82.

17. E. M. S. Maçôas, L. Khriachtchev, M. Pettersson, R. Fausto and M. Räsänen, *Phys. Chem. Chem. Phys.*, 2005, **7**, 743–749.

18. L. Khriachtchev, *J. Mol. Struct.*, 2008, **880**, 14–22.

19. M. Pettersson, E. M. S. Maçôas, L. Khriachtchev, J. Lundell, R. Fausto and M. Räsänen, *J. Chem. Phys.*, 2002, **117**, 9095–9098.

20. E. M. S. Maçôas, L. Khriachtchev, M. Pettersson, J. Juselius, R. Fausto and M. Räsänen, *J. Chem. Phys.*, 2003, **119**, 11765–11772.

21. K. Marushkevich, L. Khriachtchev, J. Lundell and M. Räsänen, *J. Am. Chem. Soc.*, 2006, **128**, 12060–12061.

22. K. Marushkevich, L. Khriachtchev, J. Lundell, A. Domanskaya and M. Räsänen, *J. Phys. Chem. A*, 2010, **114**, 3495–3502.

23. E. M. S. Maçôas, L. Khriachtchev, R. Fausto and M. Räsänen, *J. Phys. Chem. A*, 2004, **108**, 3380–3389.

24. E. M. S. Maçôas, L. Khriachtchev, M. Pettersson, R. Fausto and M. Räsänen, *J. Chem. Phys.*, 2004, **121**, 1331–1338.

25. R. F. G. Apóstolo, G. Bazsó, R. R. F. Bento, G. Tarczay and R. Fausto, *J. Mol. Struct.*, 2016, **1125**, 288–295.

26. R. F. G. Apóstolo, G. Bazsó, G. Ogruc-Ildiz, G. Tarczay and R. Fausto, *J. Chem. Phys.*, 2018, **148**, 044303.

27. E. M. S. Maçôas, L. Khriachtchev, M. Pettersson, R. Fausto and M. Räsänen, *J. Phys. Chem. A*, 2005, **109**, 3617–3625.

28. G. Bazsó, S. Góbi and G. Tarczay, *J. Phys. Chem. A*, 2012, **116**, 4823–4832.

29. E. Isoniemi, L. Khriachtchev, M. Makkonen and M. Räsänen, *J. Phys. Chem. A*, 2006, **110**, 11479–11487.

30. I. Reva, C. M. Nunes, M. Biczysko and R. Fausto, *J. Phys. Chem. A*, 2014, **119**, 2614–2627.

31. D. Gerbig and P. R. Schreiner, *J. Phys. Chem. B*, 2014, **119**, 693–703.

32. A. Halasa, L. Lapinski, I. Reva, H. Rostkowska, R. Fausto and M. J. Nowak, *J. Phys. Chem. A*, 2015, **119**, 1037–1047.

33. S. Nishino and M. Nakata, *J. Phys. Chem. A*, 2007, **111**, 7041–7047.

34. J. P. Wagner, H. Peter Reisenauer, V. Hirvonen, C.-H. Wu, J. L. Tyberg, W. D. Allen and P. R. Schreiner, *Chem. Comm.*, 2016, **52**, 7858–7861.

35. M. M. Linden, J. P. Wagner, B. Bernhardt, M. A. Bartlett, W. D. Allen and P. R. Schreiner, *J. Phys. Chem. Lett.*, 2018, **9**, 1663–1667.

36. G. Bazsó, G. Magyarfalvi and G. Tarczay, *J. Phys. Chem. A*, 2012, **116**, 10539–10547.

37. G. Bazsó, E. E. Najbauer, G. Magyarfalvi and G. Tarczay, *J. Phys. Chem. A*, 2013, **117**, 1952–1962.

38. I. Reva, M. J. Nowak, L. Lapinski and R. Fausto, *J. Chem. Phys.*, 2012, **136**, 064511.

39. L. Lapinski, I. Reva, H. Rostkowska, R. Fausto and M. J. Nowak, *J. Phys. Chem. B*, 2014, **118**, 2831–2841.

40. R. L. Redington and T. E. Redington, *J. Mol. Spectr.*, 1979, **78**, 229–247.

41. R. L. Redington T. E. Redington and J. M. Montgomery, *J. Chem. Phys.*, 2000, **113**, 2304–2318.

42. F. Madeja and M. Havenith, *J. Chem. Phys.*, 2002, **117**, 7162–7168.

43. R. J. McMahon and O. L. Chapman, *J. Am. Chem. Soc.*, 1987, **109**, 683–692.

44. N. Nakane, T. Enyo and H. Tomioka, *J. Org. Chem.*, 2004, **69**, 3538–3545.

45. D. Gerbig, H. P. Reisenauer, C.-H. Wu, D. Ley, W. D. Allen and P. R. Schreiner, *J. Am. Chem. Soc.*, 2010, **132**, 7273–7275.

46. P. R. Schreiner, H. Peter Reisenauer, F. C. Pickard IV, A. C. Simmonett, W. D. Allen, E. Mátyus and A. G. Császár, *Nature*, 2008, **453**, 906–909.

47. P. R. Schreiner, H. P. Reisenauer, D. Ley, D. Gerbig, C.-H. Wu, W. D. Allen, *Science*, 2011, **332**, 1300–1303.

48. D. Ley, D. Gerbig, J. P. Wagner, H. P. Reisenauer and P. R. Schreiner, *J. Am. Chem. Soc.*, 2011, **133**, 13614–13621.

49. S. Henkel, Y-am Huynh, P. Neuhaus, M. Winkler and W. Sander, *J. Am. Chem. Soc.*, 2012, **134**, 13204–13207.

50. D. Ley, D. Gerbig and P. R. Schreiner, *Chem. Sci.*, 2013, **4**, 677–684.

51. A. Mardyukov, H. Quanz and P. R. Schreiner, *Nat. Chem.*, 2017, **9**, 71–76.

52. A. K. Eckhardt, F. R. Erb and P. R. Schreiner, *Chem Sci.*, 2019, **10**, 802–808.

53. D. Gerbig and P. R. Schreiner, *Angew. Chem. Int. Ed.*, 2017, **56**, 9445–448.

54. C. M. Nunes, S. N. Knezz, I. Reva, R. Fausto and R. J. McMahon, *J. Am. Chem. Soc.*, 2016, **138**, 15287–15290.

55. H. Rostkowska, L. Lapinski, A. Khvorostov and M. J. Nowak, *Chem. Phys.*, 2004, **298**, 223–232.

56. J. Sarka, A. G. Császár and P. R. Schreiner, 2011, **76**, *Collect. Czech. Chemm. Commun.*, 645–667.

57. A. Halasa, L. Lapinski, H. Rostkowska and M. J. Nowak, *J. Phys. Chem. A*, 2015, **119**, 9262–9271.

58. X. Chen, Y. Zhao, H. Zhang, J. Xue and X. Zheng, *J. Phys. Chem. A,* 2015, **119**, 832–842.

59. A. D. Becke, *J. Chem. Phys.*, 1993, **98**, 5648−3652.

60. C. Lee, W. Yang and R. G. Parr, *Phys. Rev. B*, 1988, **37**, 785−789.

61. S. H. Vosko, L. Wilk and M. Nusair, *Can. J. Phys.*, 1980, **58**, 1200–1211.

62. W. J. Hehre, R. Ditchfield and J. A. Pople, *J. Chem. Phys.*, 1972, **56**, 2257−2261.

63. Gaussian 09, Revision D.01, M. J. Frisch, G. W. Trucks, H. B. Schlegel, G. E. Scuseria, M. A. Robb, J. R. Cheeseman, G. Scalmani, V. Barone, B. Mennucci, G. A. Petersson, H. Nakatsuji, M. Caricato, X. Li, H. P. Hratchian, A. F. Izmaylov, J. Bloino, G. Zheng, J. L. Sonnenberg, M. Hada, M. Ehara, K. Toyota, R. Fukuda, J. Hasegawa, M. Ishida, T. Nakajima, Y. Honda, O. Kitao, H. Nakai, T. Vreven, J. A. Montgomery, Jr., J. E. Peralta, F. Ogliaro, M. Bearpark, J. J. Heyd, E. Brothers, K. N. Kudin, V. N. Staroverov, T. Keith, R. Kobayashi, J. Normand, K. Raghavachari, A. Rendell, J. C. Burant, S. S. Iyengar, J. Tomasi, M. Cossi, N. Rega, J. M. Millam, M. Klene, J. E. Knox, J. B. Cross, V. Bakken, C. Adamo, J. Jaramillo, R. Gomperts, R. E. Stratmann, O. Yazyev, A. J. Austin, R. Cammi, C. Pomelli, J. W. Ochterski, R. L. Martin, K. Morokuma, V. G. Zakrzewski, G. A. Voth, P. Salvador, J. J. Dannenberg, S. Dapprich, A. D. Daniels, O. Farkas, J. B. Foresman, J. V. Ortiz, J. Cioslowski and D. J. Fox, Gaussian, Inc., Wallingford CT, 2013.

64. C. Y. Peng, P. Y. Ayala, H. B. Schlegel and M. J. J. Frisch, *Comput. Chem.*, 1996, **17**, 49−56.

65. K. Fukui, *Acc. Chem. Res.*, 1981, **14**, 363−368.

66. W. T. Borden, *WIREs Comput. Mol. Sci.*, 2016, **6**, 20–46.

67. J. A. Montgomery Jr., M. J. Frisch, J. W. Ochterski and G. A. Petersson, *J. Chem. Phys.*, 2000, **112**, 6532–6542.

68. L. A. Curtiss, P. C. Redfern and K. Raghavachari, *J. Chem. Phys.*, 2007, **126**, 084108.

69. L. A. Curtiss, P. C. Redfern and K. Raghavachari, *J. Chem. Phys.*, 2007, **127**, 124105.

70. S. Dapprich and G. Frenking, *Chem. Phys. Lett.*, 1993, **205**, 337–342.

71. L. Duarte, I. Reva, M. L. S. Cristiano and R. Fausto, *J. Org. Chem.*, 2013, **78**, 3271−3275.

72. A. Halasa, I. Reva, L. Lapinski, M. J. Nowak and R. Fausto, *J. Phys. Chem. A*, 2016, **120**, 2078–2088.

73. V. Guner, K. S. Khuong, A. G. Leach, P. S. Lee, M. D. Bartberger and K. N. Houk, *J. Phys. Chem. A*, 2003, **107**, 11445–11459.

74. A. Karton, R. J. O'Reilly and L. Radom, *J. Phys. Chem. A*, 2012, **116**, 4211–4221.

75. A. Karton, J. M. L. Martin, *Mol. Phys.*, 2012, **110**, 2477–2491.

76. F. Duvernay, P. Chatron-Michaud, F. Borget, D. M. Birney and T. Chiavassa, *Phys. Chem. Chem. Phys.*, 2007, **9**, 1099–1106.

77. A. J. Lopes Jesus, C. M. Nunes, I. Reva, S. M. Viera Pinto and R. Fausto, *J. Phys. Chem. A*, 2019, **123**, 4396–4405.

78. P. R. Schreiner, J. P. Wagner, H. P. Reisenauer, D. Gerbig, D. Ley, J. Sarka, A. G. Császár, A. Vaughn and W. D. Allen, *J. Am. Chem. Soc.*, 2015, **137**, 7828–7834.

79. L. Lapinski, I. Reva, H. Rostkowska, A. Halasa, R. Fausto and M. J. Nowak, *J. Phys. Chem. A*, 2013, **117**, 5251–5259.

Figure 1. Structures of the thioacetamide isomers as optimized at the B3LYP/6-311++G(3df,3pd) level of theory.

Figure 2. Structures of the thioacetamide TSs as optimized at the B3LYP/6-311++G(3df,3pd) level of theory. Only one of the mirror-image structures of both the **aC–aT** and **sC–sT** TSs, differing only in the orientation of their S–H groups, are shown.

Figure 3. (**a**) Selected regions of the mid-IR spectrum showing new bands of thiol isomers after UV irradiation of thioacetamide in an Ar matrix at 11 K; (**b**) changes in the spectrum when monitoring the spontaneous decay process overnight. Increasing bands show the formation of the respective isomer. The spectra were collected using the longpass filter with a cut-off wavenumber of 870 cm^{-1}. The filter was placed between the spectrometer light source and the cryostat and remained there also between the spectral collections; (**c**) simulated difference spectrum showing a quantitative **sC → sT** conversion. The absorptions were convoluted with Lorentzian functions (FWHM = 0.5 cm^{-1}) centered at the B3LYP/6-311++G(3df,3pd) computed wavenumbers. The computed infrared intensities of **sC** were multiplied by (−1).

Figure 4. (**a**) Kinetic decay of the band at 836 cm^{-1} (**sC**), (**b**) kinetic growth of the band at 849 cm^{-1} (**sT**) using the longpass filter with a cut-off wavenumber of 870 cm^{-1} (experiment **1a**, at 11 K).

Figure 5. Structures of the thioacetamide isomers discussed in this work. The names are shown in bold, followed by relative energies with respect to the **sT** thiol isomer. The numbers near the dashed lines represent the relative energies of the first-order TSs (with respect to the **sT** form), as well as the barrier widths (in bohr) along the respective intrinsic reaction paths [in brackets]. Energies of all the stationary points (in kJ mol^{-1}) include the zero-point vibrational energy corrections, computed at the B3LYP/6-311++G(3df,3pd) level of theory. See also Figure S8.

18

Tn

aC

aT

sC

sT

20

aC, 1.7   **aT,** 6.5

29.4 [4.35]

88.9 [2.73]   90.9 [2.60]

108.5 [2.44]

17.0 [4.66]

sC, 0.6   **sT**, 0.0

Tn, -38.4
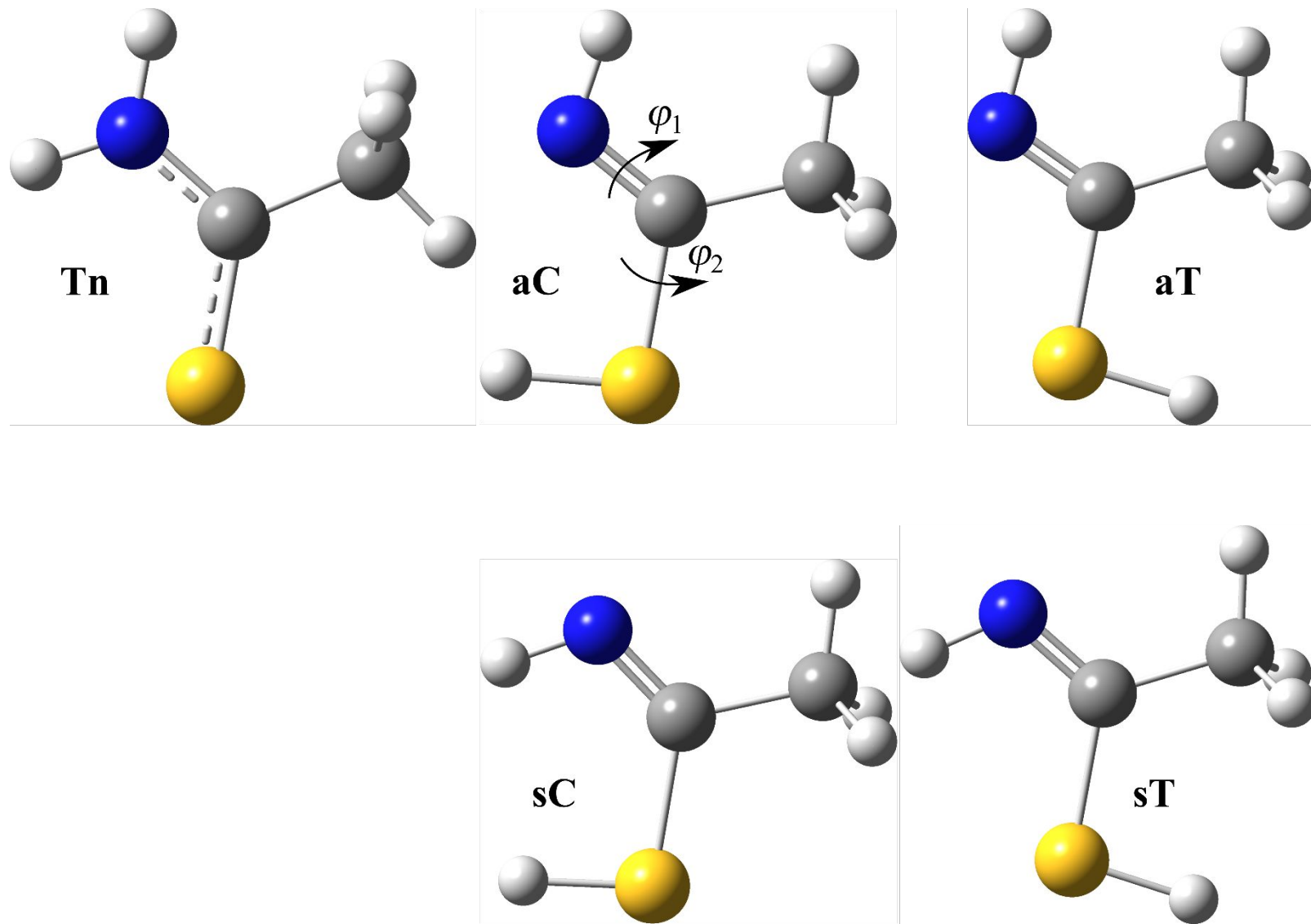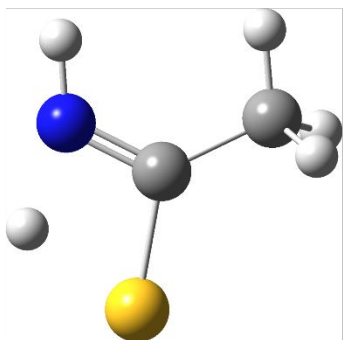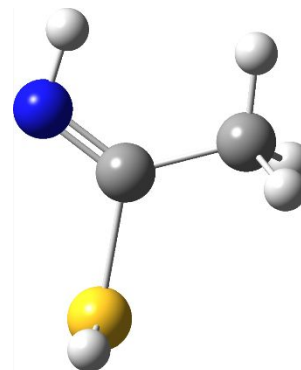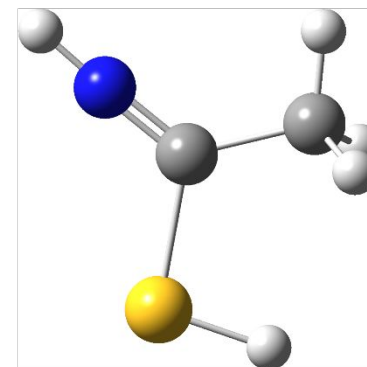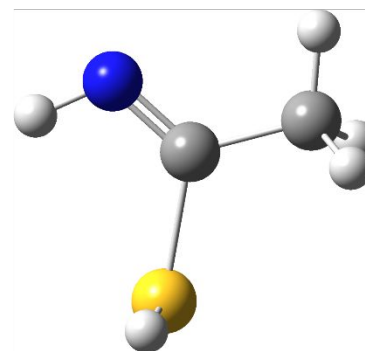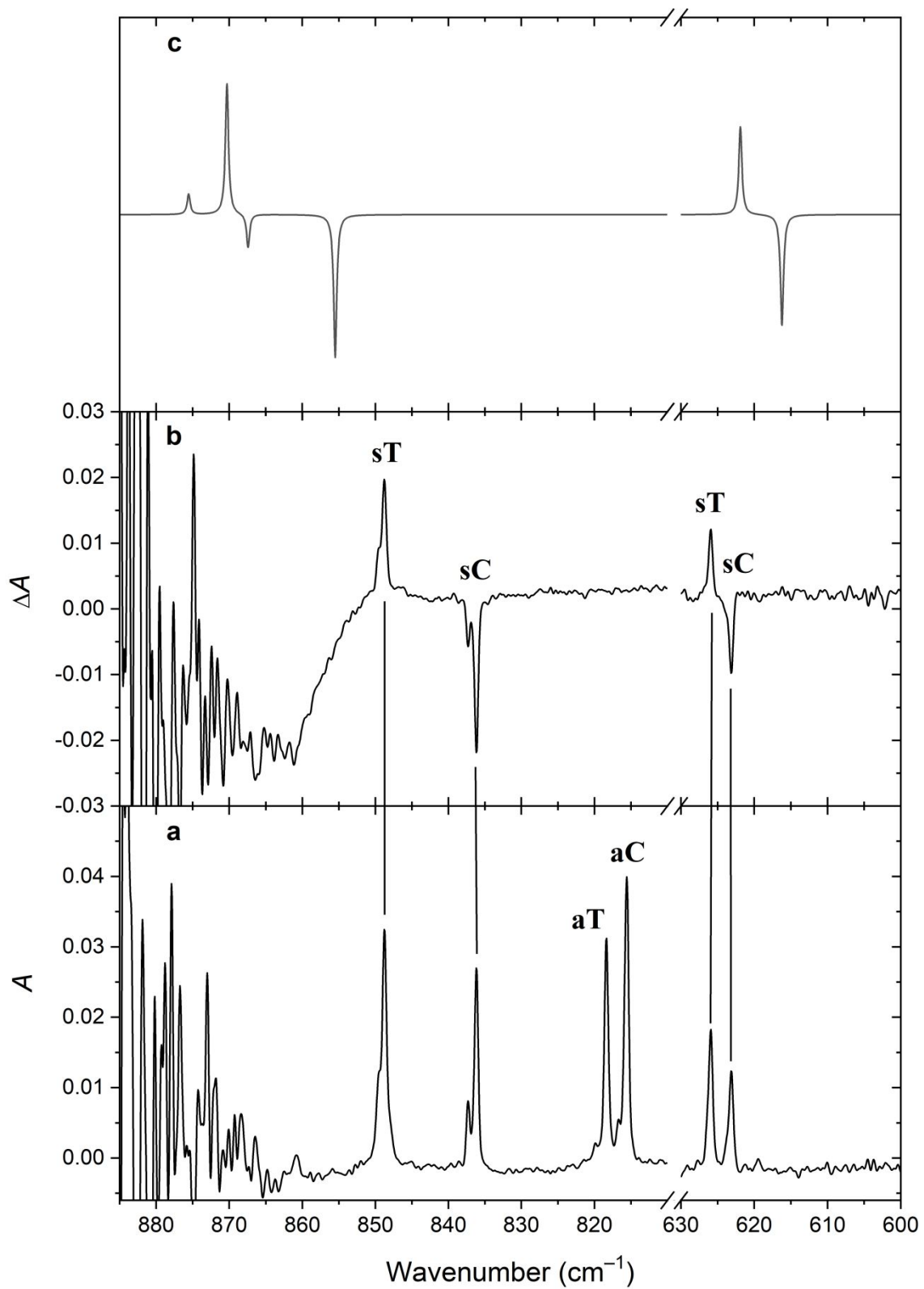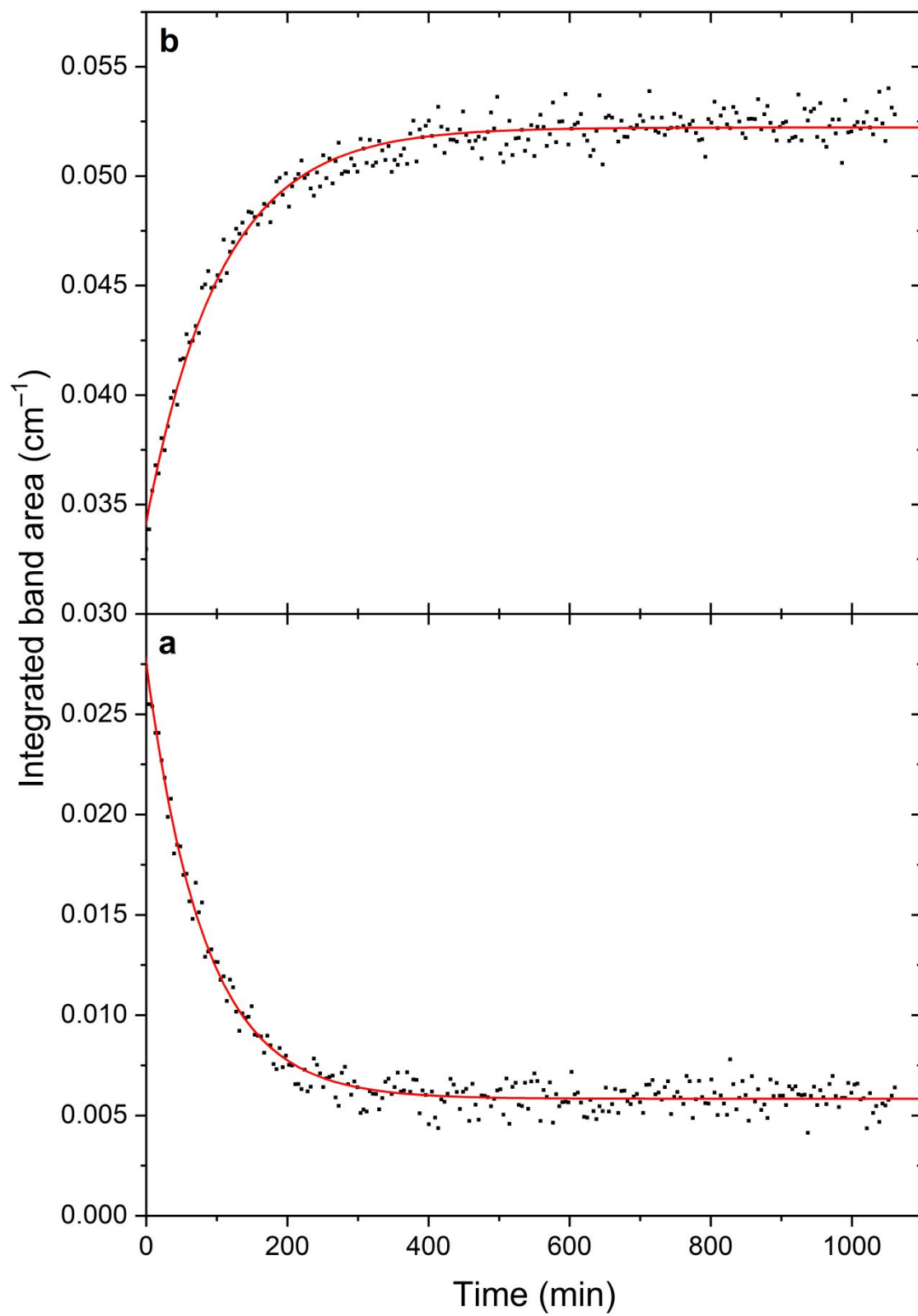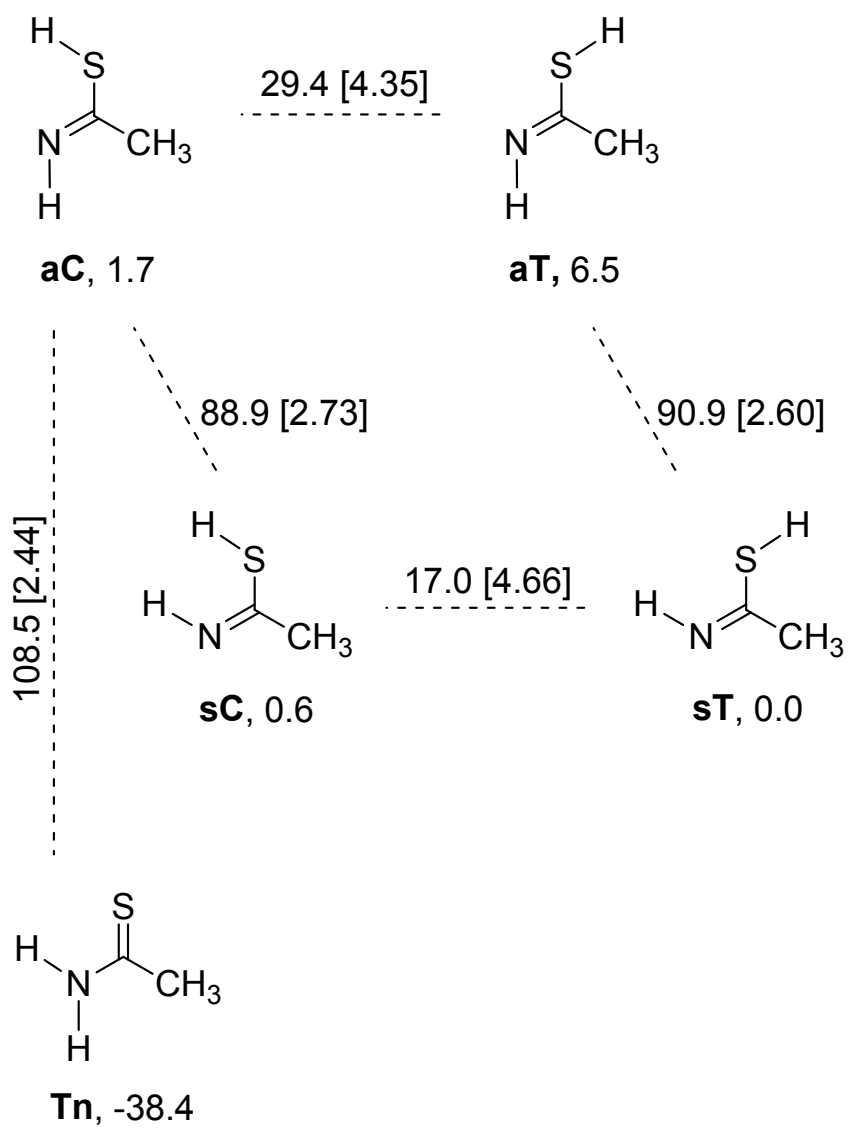
Table 1. Relative zero-point corrected energies (ΔE_{ZPE})[a] of the thioacetamide isomers (minima) and the first-order TSs computed at the B3LYP/6-311++G(3df,3pd) level of theory, as well as conformationally-relevant dihedral angles (φ_1 and φ_2).[b]

Structures	φ_1	φ_2	ΔE_{ZPE}	$\Delta\Delta E^{\#}(\rightarrow)$	$\Delta\Delta E^{\#}(\leftarrow)$
minima					
Tn	–	–	−38.4	–	–
aC	180.0	0.0	1.7	–	–
aT	180.0	180.0	6.5	–	–
sC	0.0	0.0	0.6	–	–
sT	0.0	180.0	0.0	–	–
TSs					
Tn–aC	180.0	0.0	108.5	146.9	106.8
aC–sC	−180.0	0.0	88.9	87.2	88.3
aT–sT	180.0	180.0	90.9	84.4	90.9
aC–aT–1	178.8	88.6	29.4	27.7	22.9
aC–aT–2	−178.8	−88.6	29.4	27.7	22.9
sC–sT–1	−0.6	85.1	17.0	16.4	17.0
sC–sT–2	0.6	−85.1	17.0	16.4	17.0

[a] All energies in kJ mol^{-1}, the energy of isomer **sT** was chosen as the relative zero.

[b] In degrees, φ_1 = H–N=C–S, φ_2 = H–S–C=N, see also Figure 1.

24

Table 2. Assignment of the infrared spectra of thioacetamide and its isomers isolated in an Ar matrix and spectral changes of the sample in the region of 855–500 cm^{-1}.

Wavenumber (cm^{-1})		$I_{calc.}$ [a]	Sym.	Change [b]			Approx. assign.[c]	Form[d]
Exp.	Calc.[a]			upon UV irr.	spont. (no filter)	spont. (with filter)		
850sh, 849	870.62	49.97	A"	+	+	+	τ(N–H)	**sT**
837, 836	855.98	54.64	A"	+	–	–	τ(N–H)	**sC**
820, 818	832.28	58.48	A"	+	–	0	τ(N–H)	**aT**
817, 816	829.46	54.12	A"	+	+	0	τ(N–H)	**aC**
774	–	–	A'	–	0	0	2ω(NH$_2$)	**Tn**
729	732.91	7.50	A'	–	0	0	ν(CS)	**Tn**
645	636.88	49.21	A'	+	+	0	ν(C–S)	**aC**
640	637.94	48.39	A'	+	–	0	ν(C–S)	**aT**
626	621.61	33.51	A'	+	+	+	ν(C–S)	**sT**
623	616.44	42.31	A'	+	–	–	ν(C–S)	**sC**
592	613.23	5.18	A"	–	0	0	τ(NH$_2$)	**Tn**
508	518.39	3.59	A"	–	0	0	γ(CS)	**Tn**

[a] Unscaled harmonic frequencies and absolute infrared intensities (km mol^{-1}) computed at the B3LYP/6-311++G(3df,3pd) level of theory.

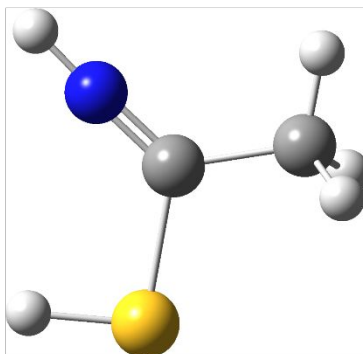[b] –/+: decrease/increase of signal, 0: no change upon irradiation

[c] ν: stretching, γ: out-of-plane bending, ω: wagging, τ: torsion

[d] Assignment based on spectral changes and computed frequencies.

Table 3. Kinetic decay/growth rates (k_d and k_g, respectively, in min^{-1}) of the thiols. Kinetic half-lives ($t_{1/2}$, in min) of the **sC** isomer calculated from the respective k_d values are also visualized.

Exp. no.	Matrix gas (temperature)	Filter	$k_d(\mathbf{sC})$	$t_{1/2}(\mathbf{sC})$	$k_g(\mathbf{s}T)$	$\mathbf{sC_f} / \mathbf{sT_f}$[a]	$k_g(\mathbf{aC})$	$k_d(\mathbf{aT})$
1a	Ar (11 K)	870 cm^{-1}	$(8.6 \pm 0.2) \times 10^{-3}$	80 ± 2	$(7.1 \pm 0.7) \times 10^{-3}$	0.11	–	–
1b	Ar (20 K)	870 cm^{-1}	$(7.4 \pm 0.5) \times 10^{-3}$	94 ± 6	$(9.5 \pm 0.2) \times 10^{-3}$	0.12	–	–
2	Ar (11 K)	870 cm^{-1} [b]	–	–	–	0.10	–	–
4b	Ar (11 K)	1960 cm^{-1}	$(1.1 \pm 0.1) \times 10^{-2}$	63 ± 6	$(1.1 \pm 0.1) \times 10^{-2}$	0.09	–	–
4a	Ar (11 K)	No filter	$(1.4 \pm 0.2) \times 10^{-2}$	50 ± 7	$(1.2 \pm 0.2) \times 10^{-2}$	0.20	$(3.0 \pm 1.0) \times 10^{-3}$	$(4.0 \pm 2.3) \times 10^{-3}$
3	Xe (11 K)	870 cm^{-1}	$(1.8 \pm 0.4) \times 10^{-2}$	39 ± 9	$(1.3 \pm 0.5) \times 10^{-2}$	0.22	–	–

[a] Ratio of the integrated band areas of the two *syn* imino forms at the end of the kinetic study.

[b] The spectrometer beam was blocked between the measurements.

26

Table 4. Tunneling rates of the thiol forms computed using the WKB approximation and based on intrinsic reaction paths calculated at the B3LYP/6-311++G(3df,3pd) level of theory.

Process	w $(10^{-10}$ m$)$	$V_0{-}E$ (J)	v (s^{-1})	$t_{1/2}$ (s)
aC → Tn	1.29	1.78×10^{-19}	2.55×10^{13}	8.63×10^{6}
aC → sC	1.44	1.45×10^{-19}	3.90×10^{13}	9.00×10^{6}
aT → sT	1.37	1.41×10^{-19}	3.90×10^{13}	4.33×10^{5}
aT → aC	2.30	3.82×10^{-20}	7.35×10^{12}	8.27×10^{3}
sC → sT	2.47	2.73×10^{-20}	8.35×10^{12}	1.79×10^{2}

27

Tn

aC φ_1 φ_2

aT

sC

sT
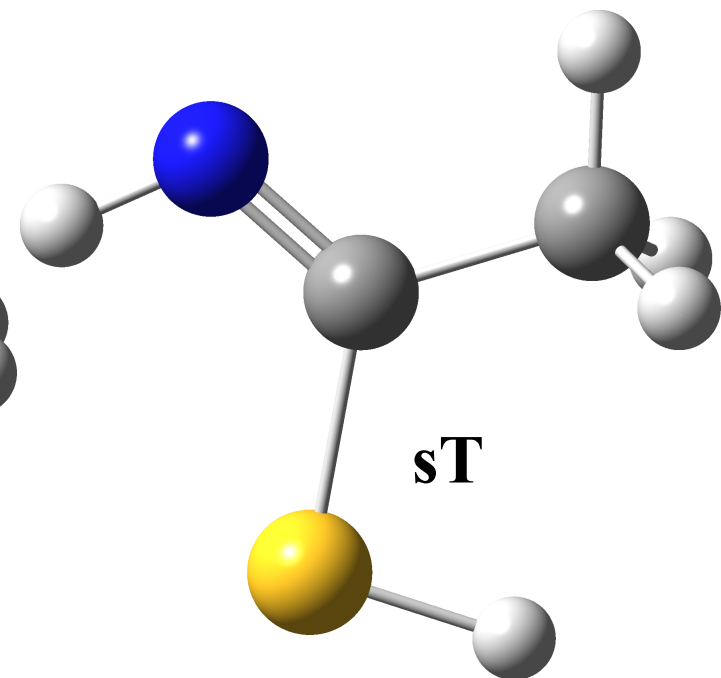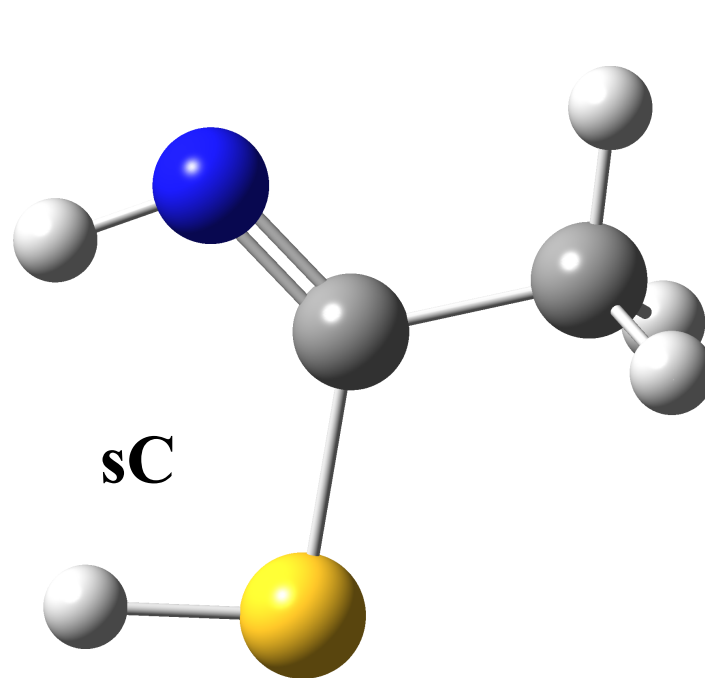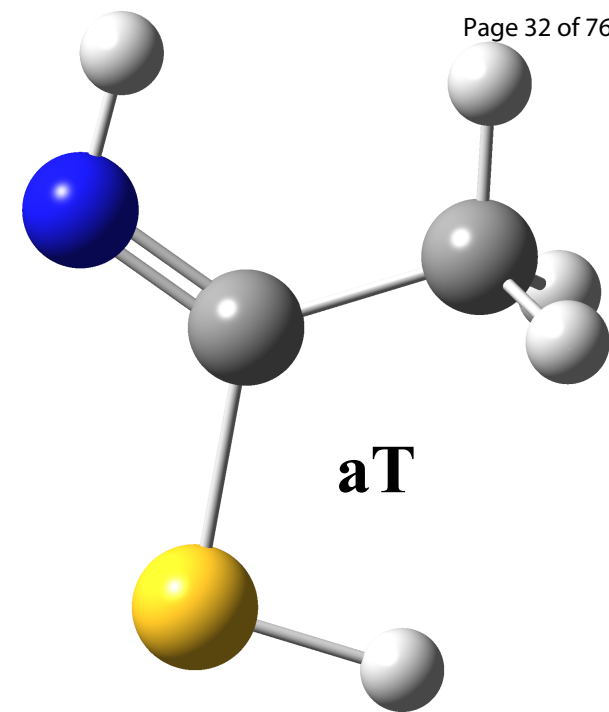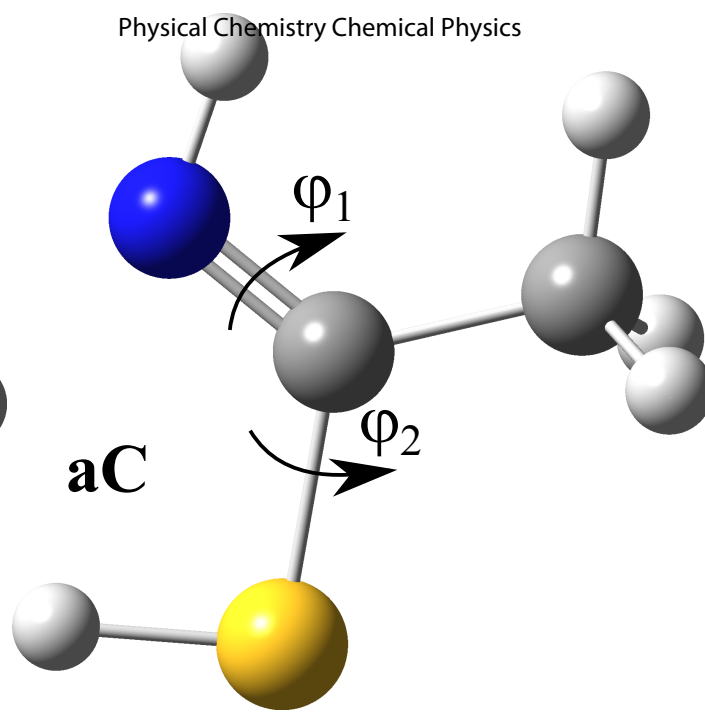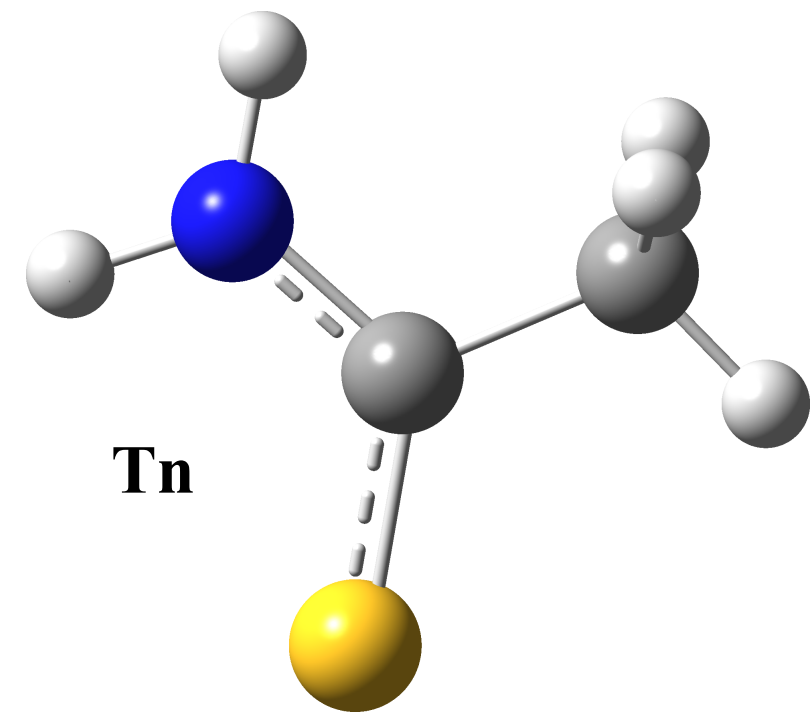
Tn
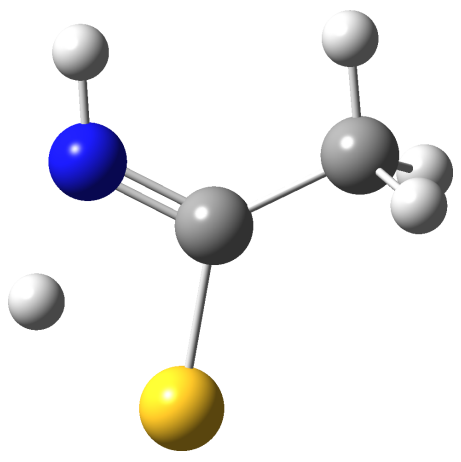
aC
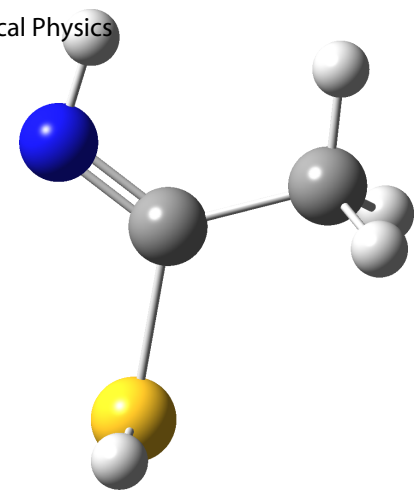
aT

sC

sT
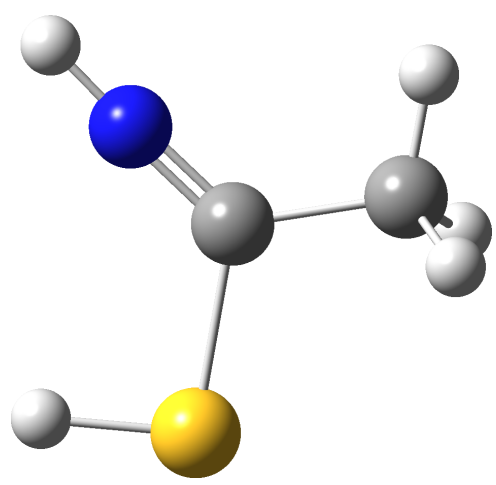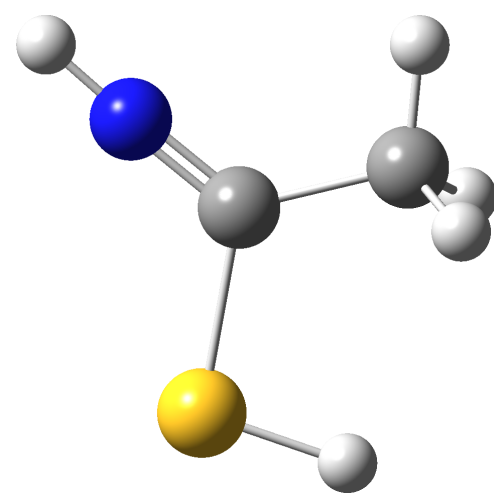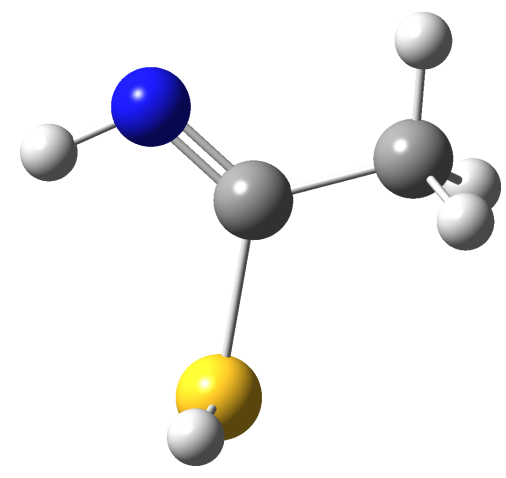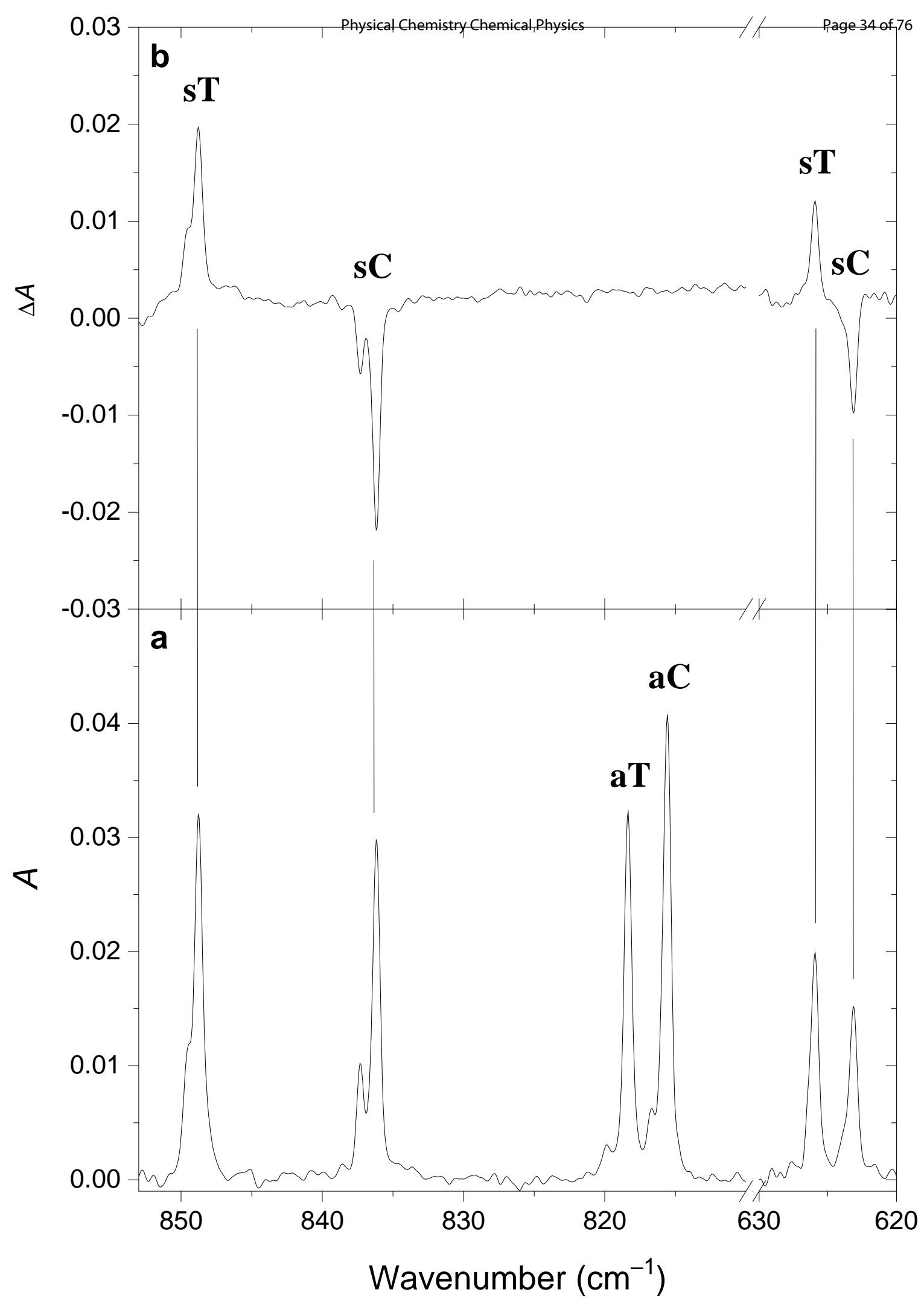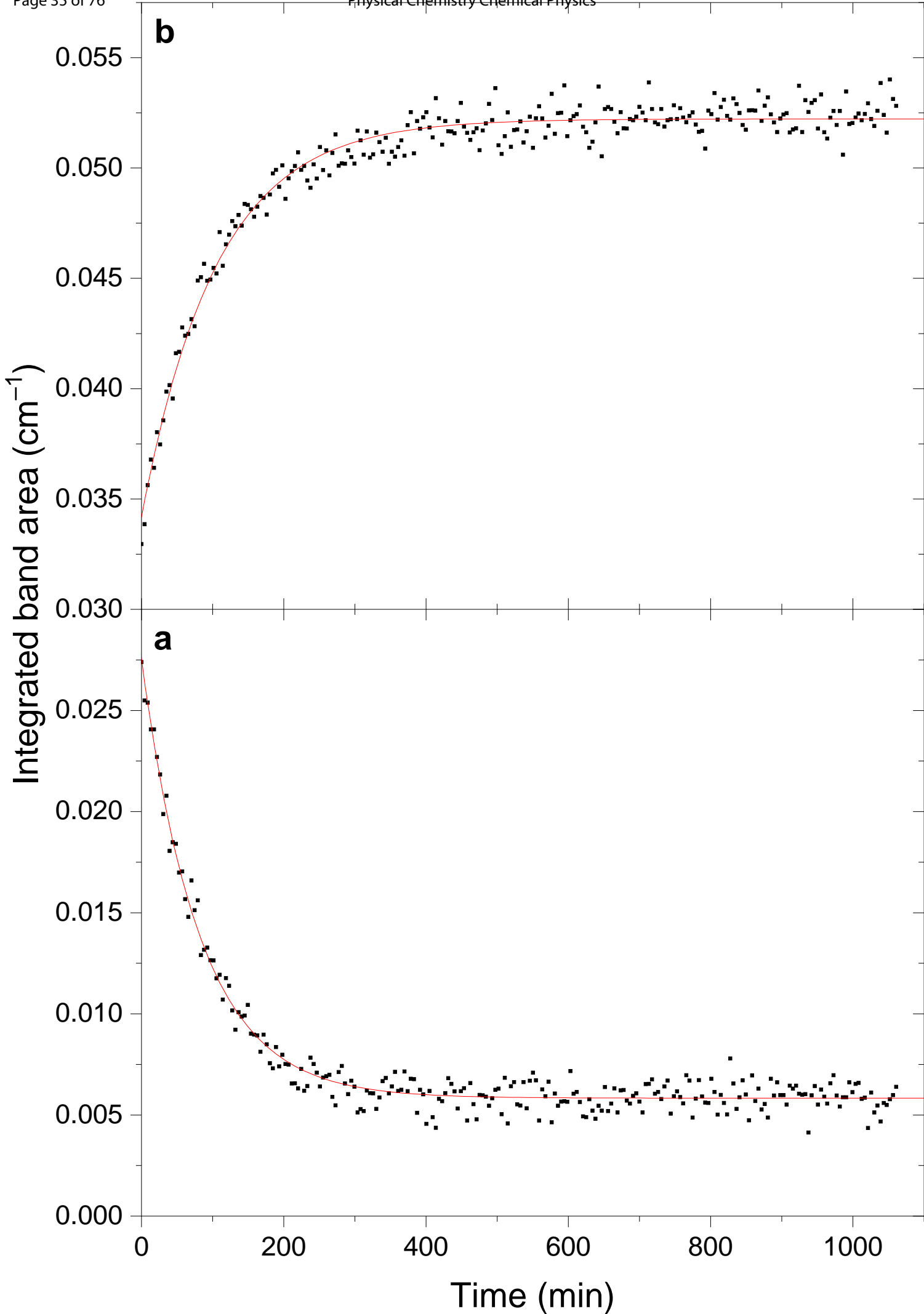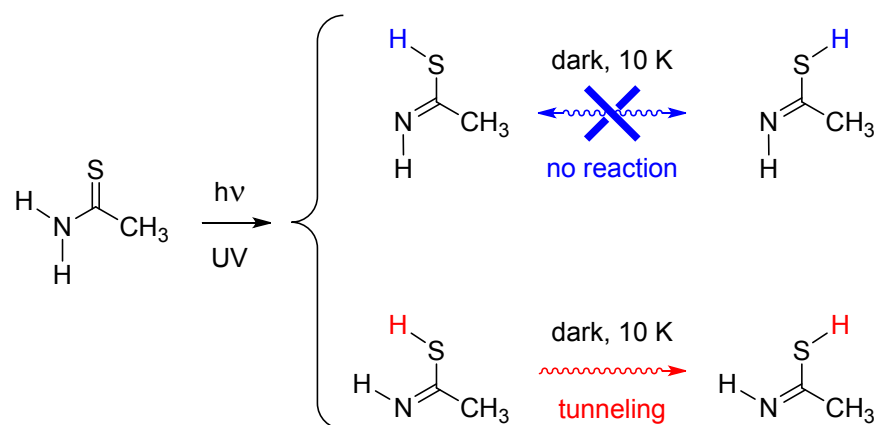
Rotamerization of the S–H group via hydrogen tunneling in one of the thiol isomers of matrix-isolated thioacetamide is reported.

Electronic Supplementary Information for

S–H Rotamerization via Tunneling in a Thiol Form of Thioacetamide

Sándor Góbi[a,*], Cláudio M. Nunes[a], Igor Reva[a], György Tarczay[b,c], and Rui Fausto[a]

[a] *CQC, Department of Chemistry, University of Coimbra, 3004–535, Coimbra, Portugal*

[b] *Laboratory of Molecular Spectroscopy, Institute of Chemistry, Eötvös Loránd University, H–1518 Budapest, Hungary*

[c] *MTA-ELTE Lendület Laboratory Astrochemistry Research Group, Institute of Chemistry, Eötvös Loránd University, H–1518 Budapest, Hungary*

*Corresponding author: sgobi@qui.uc.pt
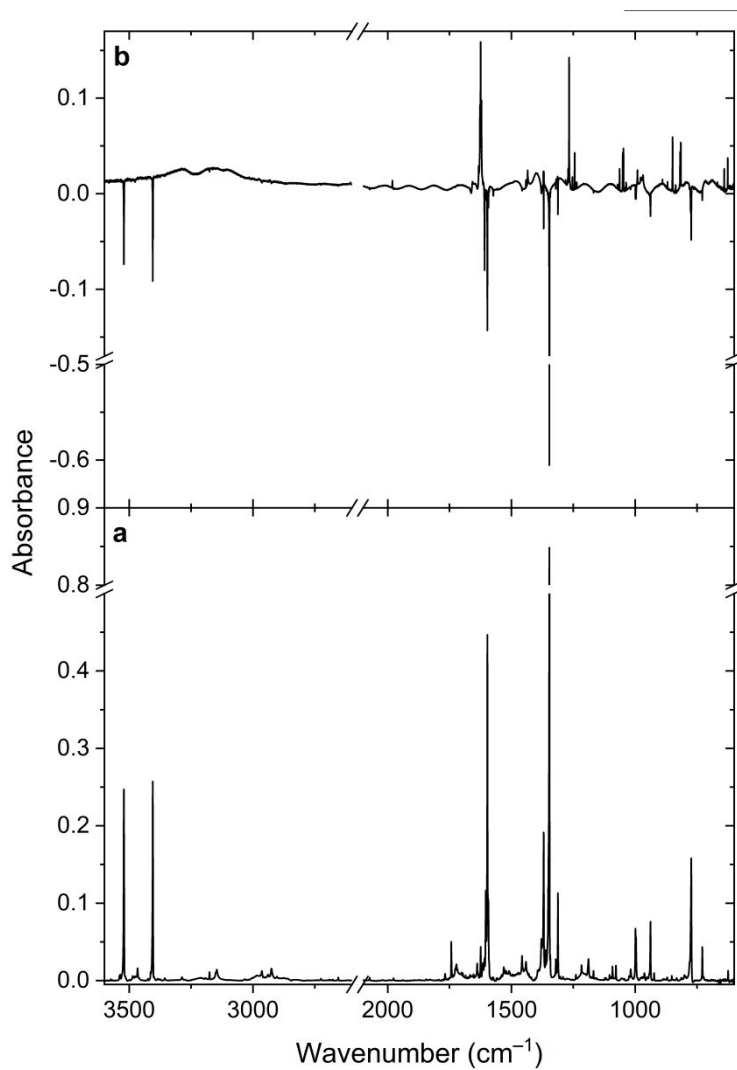
Figure S1. (a) Mid-IR spectrum of the thioacetamide monomers isolated in an Ar matrix at 11 K, collected immediately after the deposition of the sample. **(b)** Changes in the mid-IR spectrum of matrix-isolated thioacetamide upon UV irradiation ($\lambda = 269$ nm for 3 min). Positive bands grow upon the irradiation.
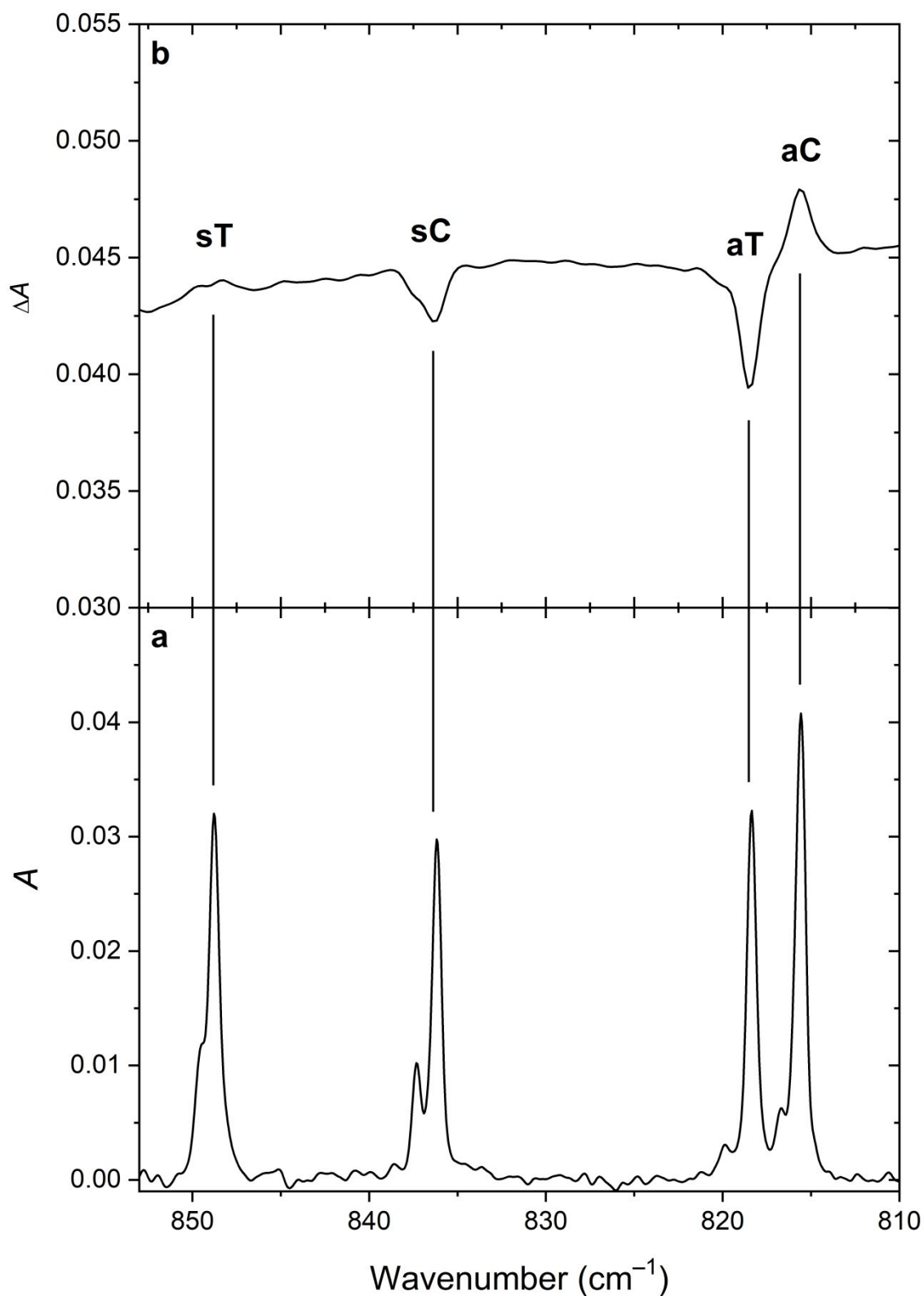
Figure S2. (**a**) Fragment of the Mid-IR spectrum (855–810 cm^{-1} region) of the thioacetamide monomers isolated in an Ar matrix at 11 K immediately after UV irradiation. (**b**) Changes in the mid-IR spectrum of matrix-isolated thioacetamide when no filter was used during the collection of spectra after exposing the sample to the spectrometer beam source for 217 min.
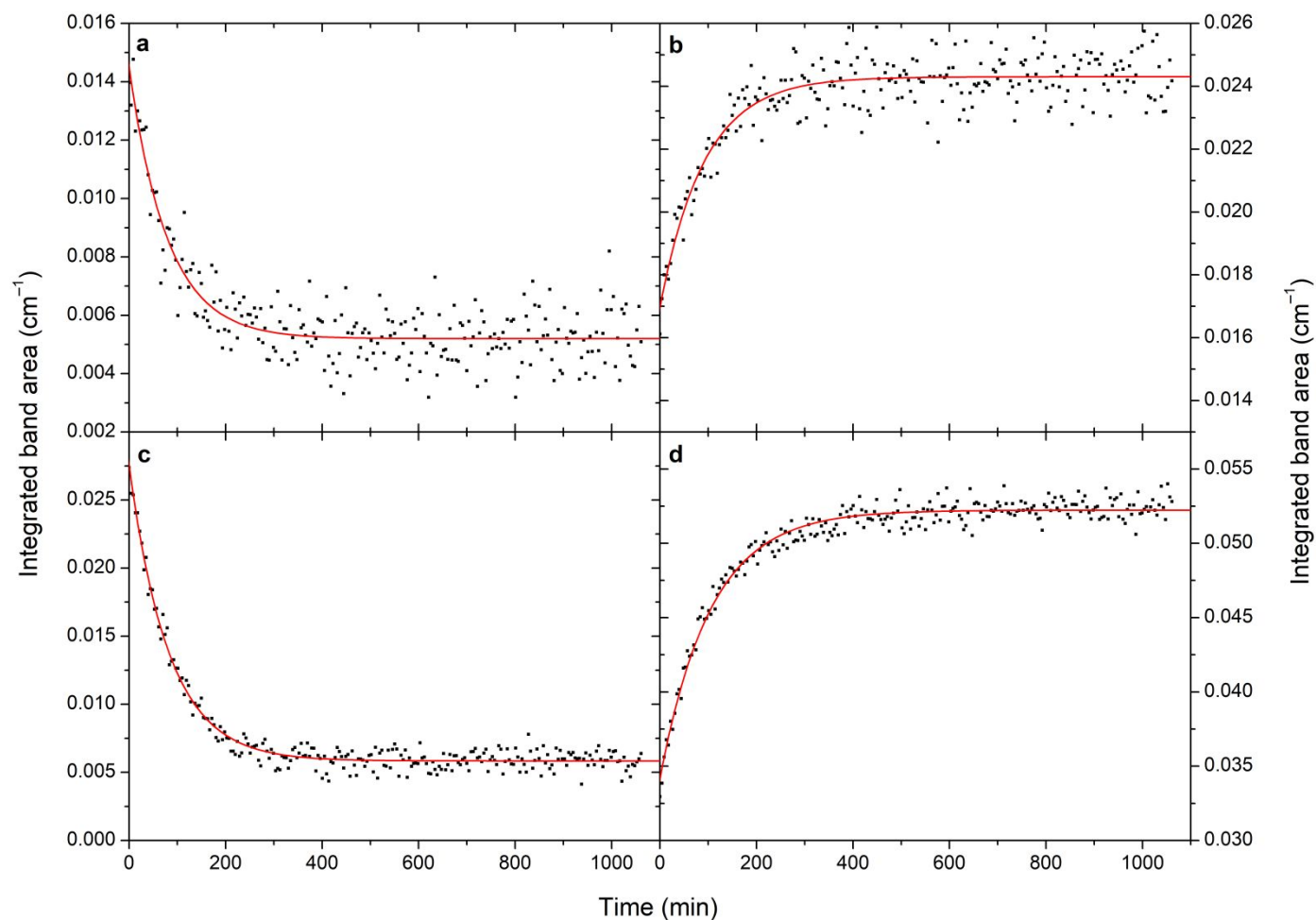
Figure S3. (**a**) Kinetic decay curve of the band at 623 cm^{-1} (**sC**), (**b**) kinetic growth curve of the band at 626 cm^{-1} (**sT**), (**c**) kinetic decay curve of the band at 836 cm^{-1} (**sC**), (**d**) kinetic growth curve of the band at 849 cm^{-1} (**sC**). The spectra were recorded using the longpass filter with a cut-off wavenumber of 870 cm^{-1} (experiment **1a**, at 11 K).
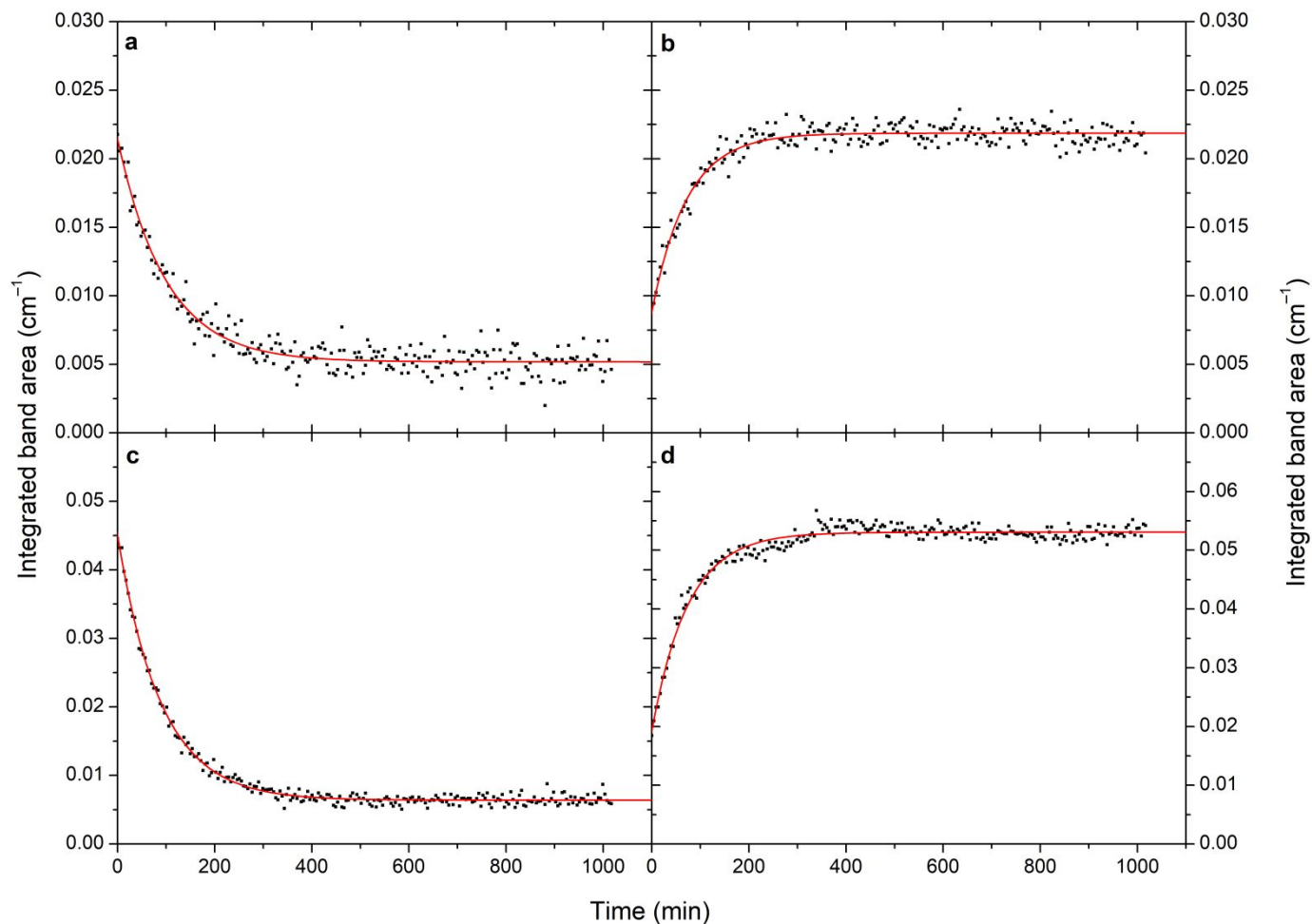
Figure S4. (a) Kinetic decay curve of the band at 620 cm^{-1} (**sC**), (**b**) kinetic growth curve of the band at 623 cm^{-1} (**sT**), (**c**) kinetic decay curve of the band at 835 cm^{-1} (**sC**), (**d**) kinetic growth curve of the band at 848 cm^{-1} (**sT**), in Ar matrix at 20 K. The spectra were recorded using the longpass filter with the cut-off wavenumber of 870 cm^{-1} (experiment **1b**).
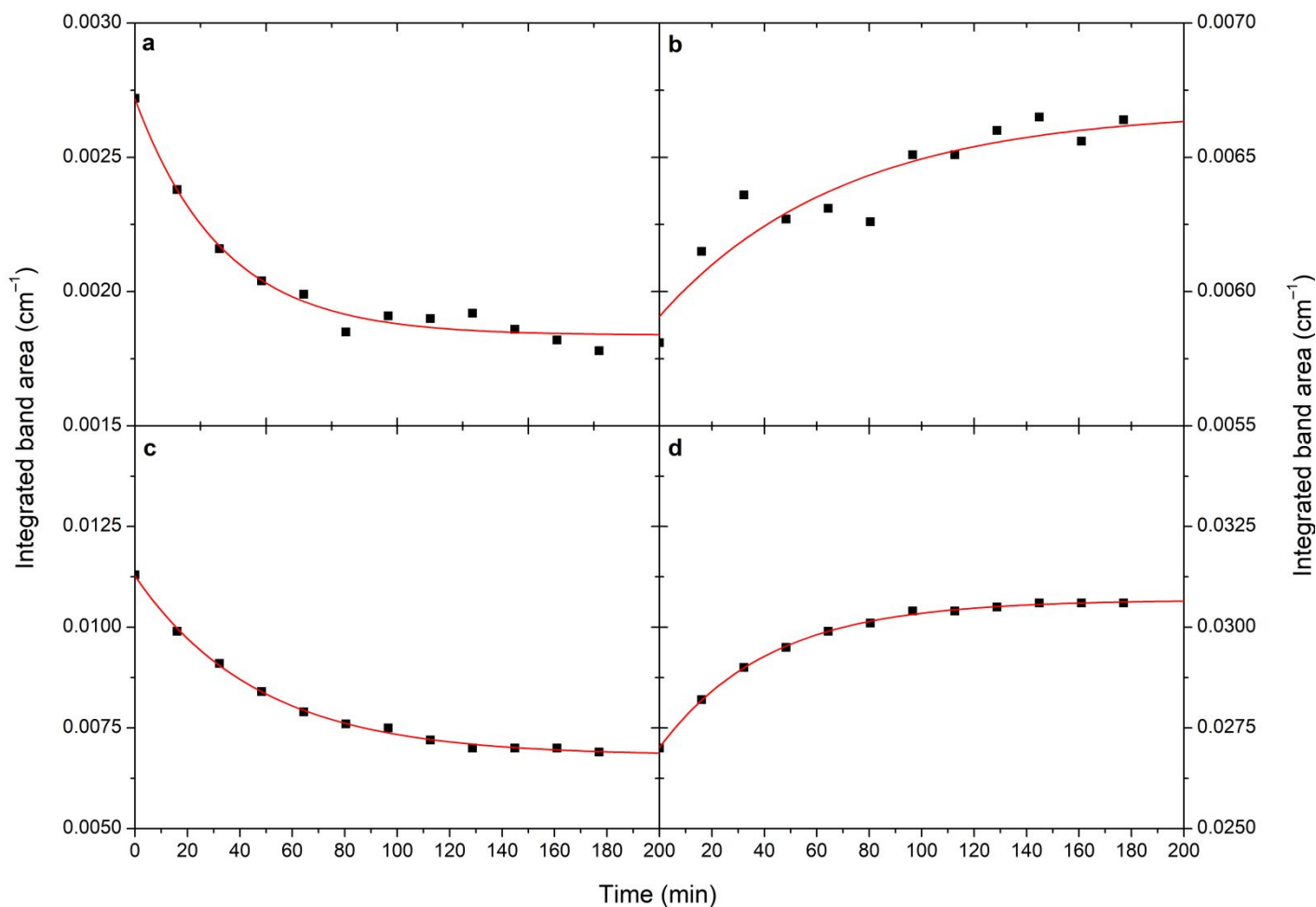
Figure S5. (**a**) Kinetic decay curve of the band at 623 cm^{-1} (**sC**), (**b**) kinetic growth curve of the band at 626 cm^{-1} (**sT**), (**c**) kinetic decay curve of the band at 836 cm^{-1} (**sC**), (**d**) kinetic growth curve of the band at 849 cm^{-1} (**sT**), in Xe matrix at 11 K. The spectra were recorded using the longpass filter with the cut-off wavenumber of 870 cm^{-1} (experiment **3**).
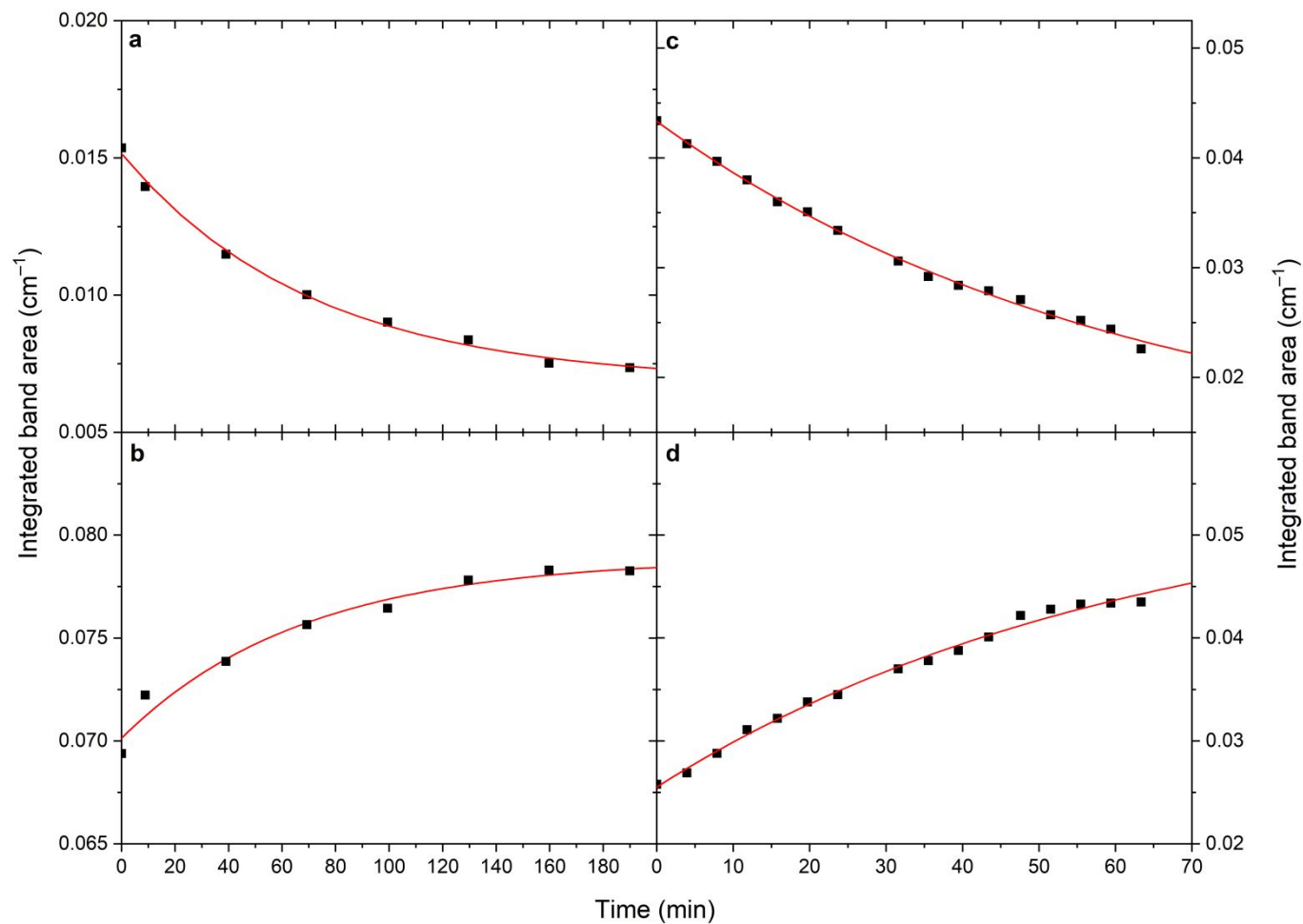
Figure S6. (**a**) Kinetic decay curve of the band at 836 cm^{-1} (**sC**), (**b**) kinetic growth curve of the band at 849 cm^{-1} (**sT**), in Ar matrix at 11 K. The spectra were recorded using the longpass filter with the cut-off wavenumber of 1960 cm^{-1} (experiment **4a**). (**c, d**) plots the curves of the same bands when the measurement was repeated during the same experiment.
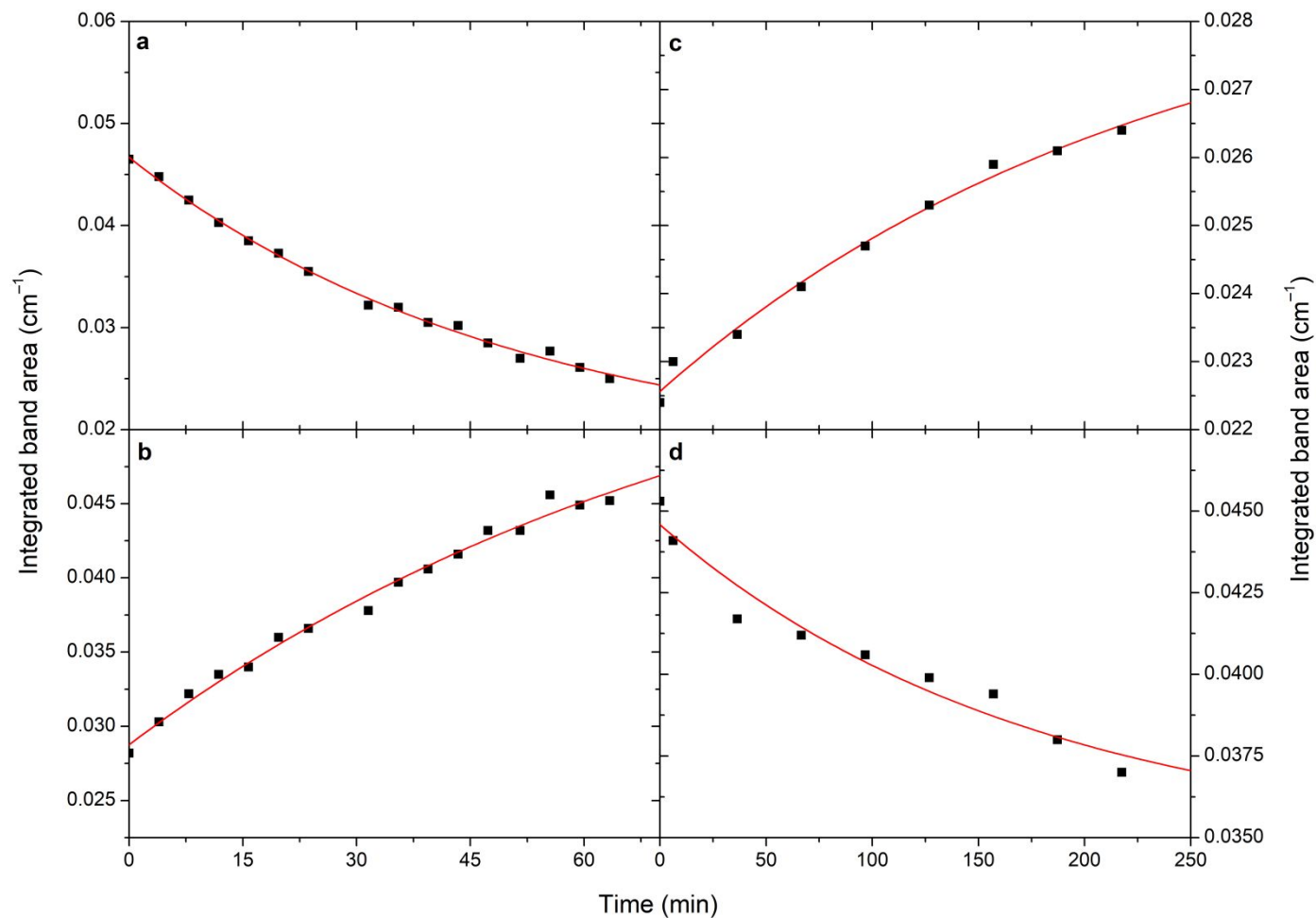
Figure S7. (a) Kinetic decay curve of the band at 836 cm^{-1} (**sC**), (**b**) kinetic growth curve of the band at 849 cm^{-1} (**sT**), (**c**) kinetic growth curve of the band at 816 cm^{-1} (**aC**), (**d**) kinetic decay curve of the band at 818 cm^{-1} (**aT**), in Ar matrix at 11 K. The spectra were recorded without using any filter (experiment **4b**).

7
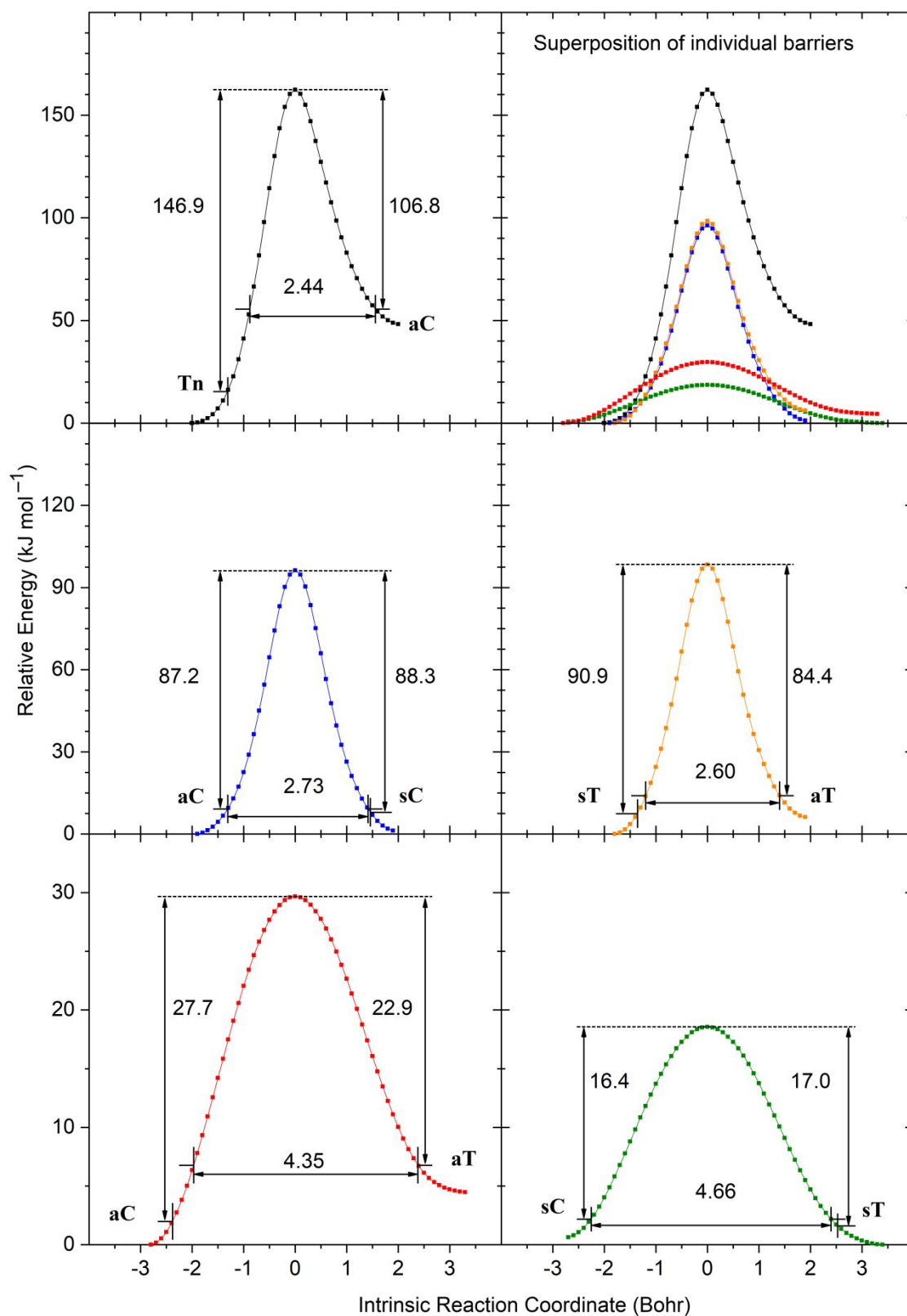
Figure S8. IRC pathways between the thioacetamide isomers as calculated at the B3LYP/6-311++G(3df,3pd) level of theory. The colors in the top-right panel displaying the superimposed profiles all correspond to those of each individual profile in the rest of the panels.

Table S1. Cartesian coordinates (in Å) of the **Tn** tautomer as optimized at the B3LYP/6-311++G(3df,3pd) level of theory.

Atom	X	Y	Z
C	0.000000	0.283881	0.000000
S	-0.168012	-1.358478	0.000000
N	-1.057753	1.116049	0.000000
H	-1.987466	0.731082	0.000000
H	-0.947449	2.116062	0.000000
C	1.337009	0.980343	0.000000
H	1.432099	1.618176	0.882142
H	2.141122	0.254466	0.000000
H	1.432099	1.618176	-0.882142

Table S2. Unscaled harmonic vibrational frequencies (E_{harm}, in cm^{-1}) and absolute IR intensities (I, in km mol^{-1}) of the **Tn** tautomer as calculated at the B3LYP/6-311+G(d,p) level of theory.

Mode number	E_{harm}	I
1	3694.4179	37.2886
2	3564.7349	42.0762
3	3166.2241	1.5240
4	3071.6932	8.2463
5	3021.3099	18.8524
6	1637.5680	154.9839
7	1488.0402	8.2178
8	1481.5459	10.3812
9	1403.8862	38.2732
10	1376.5186	244.9253
11	1322.2294	40.7817
12	1037.6401	0.2203
13	1021.8841	24.1543
14	987.7281	16.0086
15	732.4758	7.6178
16	612.9309	5.3280
17	518.0586	3.7582
18	427.2914	1.1822
19	378.2104	1.9831
20	337.2837	157.3861
21	31.7943	0.0078

Table S3. Cartesian coordinates (in Å) of the **aC** isomer as optimized at the B3LYP/6-311++G(3df,3pd) level of theory.

Atom	X	Y	Z
C	0.000000	0.476229	0.000000
S	-0.340048	-1.273389	0.000000
N	-0.955276	1.305784	0.000000
H	-0.610233	2.264863	0.000000
C	1.476471	0.781276	0.000000
H	1.957092	0.350525	0.879350
H	1.957092	0.350525	-0.879350
H	1.640109	1.857275	0.000000
H	-1.675181	-1.134480	0.000000

Table S4. Unscaled harmonic vibrational frequencies (E_{harm}, in cm^{-1}) and absolute IR intensities (I, in km mol^{-1}) of the **aC** isomer as calculated at the B3LYP/6-311+G(d,p) level of theory.

Mode number	E_{harm}	I
1	3455.0698	1.5990
2	3118.9390	11.7739
3	3095.0491	4.1593
4	3035.0141	5.5051
5	2686.1431	1.3681
6	1680.8891	149.3842
7	1482.4249	22.6937
8	1472.7704	11.5825
9	1406.1832	14.0646
10	1299.3493	69.2782
11	1070.3380	52.2207
12	1063.9286	5.1831
13	996.4669	53.5051
14	851.8389	13.7590
15	828.7418	53.9772
16	636.6275	49.1557
17	501.3818	0.0755
18	449.8539	6.9078
19	339.8745	18.0836
20	325.2994	4.3443
21	97.8543	0.4673

Table S5. Cartesian coordinates (in Å) of the **aT** isomer as optimized at the B3LYP/6-311++G(3df,3pd) level of theory.

Atom	X	Y	Z
C	0.000000	0.479605	0.000000
S	-0.502335	-1.232590	0.000000
N	-0.937876	1.328045	0.000000
H	-0.578649	2.280874	0.000000
C	1.480764	0.759055	0.000000
H	1.954708	0.323926	0.880650
H	1.954708	0.323926	-0.880650
H	1.659551	1.833381	0.000000
H	0.727594	-1.768943	0.000000

Table S6. Unscaled harmonic vibrational frequencies (E_{harm}, in cm^{-1}) and absolute IR intensities (I, in km mol^{-1}) of the **aT** isomer as calculated at the B3LYP/6-311+G(d,p) level of theory.

Mode number	E_{harm}	I
1	3469.6854	2.8136
2	3112.0676	14.5335
3	3095.9082	4.6867
4	3032.6044	6.8796
5	2687.7799	1.1906
6	1682.4660	166.0005
7	1482.8715	17.6961
8	1475.2210	11.4980
9	1403.4970	12.1004
10	1300.0307	61.0301
11	1065.6938	65.2176
12	1064.8786	5.2834
13	1011.4560	50.2947
14	896.7393	12.7192
15	831.9264	58.2396
16	638.0009	48.3015
17	506.9022	0.9946
18	433.6786	3.0692
19	340.0875	0.7125
20	245.1554	4.9926
21	164.2887	0.0976

3

Table S7. Cartesian coordinates (in Å) of the **sC** isomer as optimized at the B3LYP/6-311++G(3df,3pd) level of theory.

Atom	X	Y	Z
C	0.000000	0.500945	0.000000
S	-0.302135	-1.274433	0.000000
N	-0.862430	1.423716	0.000000
H	-1.823152	1.089375	0.000000
C	1.470814	0.812772	0.000000
H	1.953845	0.385691	0.879943
H	1.953845	0.385691	-0.879943
H	1.604685	1.890715	0.000000
H	-1.642929	-1.208857	0.000000

Table S8. Unscaled harmonic vibrational frequencies (E_{harm}, in cm^{-1}) and absolute IR intensities (I, in km mol^{-1}) of the **sC** isomer as calculated at the B3LYP/6-311+G(d,p) level of theory.

Mode number	E_{harm}	I
1	3481.3760	5.0620
2	3143.3598	4.6651
3	3093.4306	5.4264
4	3038.7526	5.4430
5	2679.1971	1.1441
6	1693.5949	134.0084
7	1478.6504	12.1570
8	1473.9888	11.8748
9	1405.6028	13.7739
10	1266.4270	233.9674
11	1078.9905	25.8644
12	1069.5359	3.9606
13	996.4691	9.0763
14	867.4159	12.8501
15	855.4898	54.3986
16	616.2180	42.3314
17	493.4231	2.5792
18	442.8079	13.4119
19	328.2438	2.8180
20	278.6584	8.0265
21	105.6295	1.3377

Table S9. Cartesian coordinates (in Å) of the **sT** isomer as optimized at the B3LYP/6-311++G(3df,3pd) level of theory.

Atom	X	Y	Z
C	0.000000	0.499620	0.000000
S	-0.446990	-1.241737	0.000000
N	-0.871789	1.414649	0.000000
H	-1.829281	1.067159	0.000000
C	1.466086	0.824168	0.000000
H	1.953124	0.404140	0.881033
H	1.953124	0.404140	-0.881033
H	1.588921	1.904043	0.000000
H	0.791964	-1.756953	0.000000

Table S10. Unscaled harmonic vibrational frequencies (E_{harm}, in cm^{-1}) and absolute IR intensities (I, in km mol^{-1}) of the **sT** isomer as calculated at the B3LYP/6-311+G(d,p) level of theory.

Mode number	E_{harm}	I
1	3466.4948	4.6467
2	3136.9600	6.4429
3	3093.3999	6.1605
4	3036.9686	6.3858
5	2684.1467	0.3138
6	1690.3755	139.1256
7	1481.1225	11.9684
8	1474.5135	8.1855
9	1403.8575	12.3466
10	1283.2580	229.8708
11	1076.7845	23.9269
12	1070.8868	4.5367
13	995.9720	7.2725
14	875.5497	7.7667
15	870.3081	49.8493
16	621.8946	33.4617
17	497.0180	3.8761
18	421.1523	14.4722
19	334.5616	0.9257
20	203.5083	16.5083
21	170.3821	0.0001

Table S11. Cartesian coordinates (in Å) of the **Tn–aC** transition state as optimized at the B3LYP/6-311++G(3df,3pd) level of theory.

Atom	X	Y	Z
C	0.000000	0.399719	0.000000
S	-0.013254	-1.326561	0.000000
N	-1.239201	0.791533	0.000000
H	-1.488376	-0.573544	0.000000
H	-1.470280	1.783067	0.000000
C	1.210035	1.272362	0.000000
H	1.820856	1.057319	0.876566
H	1.820856	1.057319	-0.876566
H	0.943203	2.327593	0.000000

Table S12. Unscaled harmonic vibrational frequencies (E_{harm}, in cm^{-1}) and absolute IR intensities (I, in km mol^{-1}) of the **Tn–aC** transition state as calculated at the B3LYP/6-311+G(d,p) level of theory.

Mode number	E_{harm}	I
1	3458.6054	1.5593
2	3121.1513	9.7801
3	3106.6354	1.2513
4	3044.2682	3.6541
5	1786.7239	2.4690
6	1571.9781	183.6614
7	1474.1668	56.4747
8	1471.1220	12.1202
9	1408.1544	20.3981
10	1321.6629	97.2727
11	1093.8859	52.5734
12	1050.8489	1.8023
13	978.3773	36.0427
14	909.3064	2.3538
15	705.8478	27.1584
16	620.8459	82.0744
17	600.3002	8.6235
18	462.9283	15.1006
19	334.2143	1.9633
20	105.8606	0.6240
21	i 1709.4957	1017.7205

6

Table S13. Relative energies (ΔE, in hartree) for the minimum-energy path along the intrinsic reaction coordinate (IRC, in bohr) originating from the **Tn–aC** transition state (IRC = 0) as calculated at the B3LYP/6-311++G(3df,3pd) level of theory.

	ΔE	IRC
1	-0.06183	-2.00567
2	-0.06183	-1.99732
3	-0.06173	-1.89747
4	-0.06144	-1.79779
5	-0.06094	-1.69820
6	-0.06020	-1.59862
7	-0.05914	-1.49894
8	-0.05766	-1.39915
9	-0.05570	-1.29930
10	-0.05317	-1.19941
11	-0.05001	-1.09949
12	-0.04619	-0.99956
13	-0.04169	-0.89962
14	-0.03652	-0.79968
15	-0.03076	-0.69975
16	-0.02458	-0.59981
17	-0.01828	-0.49986
18	-0.01231	-0.39990
19	-0.00714	-0.29993
20	-0.00321	-0.19996
21	-0.00080	-0.10000
22	0.00000	0.00000
23	-0.00075	0.10000
24	-0.00281	0.19996
25	-0.00586	0.29992
26	-0.00951	0.39987
27	-0.01340	0.49980
28	-0.01725	0.59972
29	-0.02090	0.69964
30	-0.02429	0.79958
31	-0.02741	0.89955
32	-0.03023	0.99952
33	-0.03275	1.09950
34	-0.03499	1.19948
35	-0.03694	1.29945
36	-0.03861	1.39942
37	-0.04002	1.49939
38	-0.04117	1.59936
39	-0.04208	1.69932
40	-0.04276	1.79927
41	-0.04322	1.89921
42	-0.04349	1.99908

Table S14. Cartesian coordinates (in Å) of the **aC–sC** transition state as optimized at the B3LYP/6-311++G(3df,3pd) level of theory.

Atom	X	Y	Z
C	0.000000	0.529086	0.000000
S	-0.324365	-1.298204	0.000000
N	-0.879365	1.374982	0.000000
H	-1.567603	2.084164	0.000000
C	1.496028	0.768415	0.000000
H	1.696360	1.836364	0.000000
H	1.949945	0.309975	0.879571
H	1.949945	0.309975	-0.879571
H	-1.659417	-1.179089	0.000000

Table S15. Unscaled harmonic vibrational frequencies (E_{harm}, in cm^{-1}) and absolute IR intensities (I, in km mol^{-1}) of the **aC–sC** transition state as calculated at the B3LYP/6-311+G(d,p) level of theory.

Mode number	E_{harm}	I
1	3916.1249	418.0402
2	3138.2645	10.2968
3	3096.7924	4.6549
4	3036.7417	4.6778
5	2696.4242	0.3645
6	1831.7974	382.4181
7	1475.5256	12.1439
8	1473.8936	12.5558
9	1388.9953	13.1302
10	1105.1410	72.7234
11	1027.9604	0.0764
12	983.1959	42.2648
13	810.7488	19.4350
14	573.0857	80.5509
15	497.4386	0.0006
16	411.5041	25.9257
17	407.3064	101.2074
18	325.5971	2.6200
19	316.5144	15.3248
20	31.5039	1.3730
21	i 1061.0271	190.2959

8

Table S16. Relative energies (ΔE, in hartree) for the minimum-energy path along the intrinsic reaction coordinate (IRC, in bohr) originating from the **aC–sC** transition state (IRC = 0) as calculated at the B3LYP/6-311++G(3df,3pd) level of theory.

	ΔE	IRC
1	-0.03667	-1.89740
2	-0.03650	-1.79771
3	-0.03617	-1.69784
4	-0.03567	-1.59794
5	-0.03499	-1.49806
6	-0.03413	-1.39822
7	-0.03306	-1.29844
8	-0.03173	-1.19867
9	-0.03009	-1.09888
10	-0.02808	-0.99905
11	-0.02566	-0.89919
12	-0.02280	-0.79932
13	-0.01953	-0.69945
14	-0.01591	-0.59957
15	-0.01212	-0.49966
16	-0.00838	-0.39974
17	-0.00501	-0.29980
18	-0.00232	-0.19987
19	-0.00059	-0.09994
20	0.00000	0.00000
21	-0.00059	0.09994
22	-0.00227	0.19986
23	-0.00484	0.29980
24	-0.00804	0.39973
25	-0.01156	0.49965
26	-0.01512	0.59955
27	-0.01851	0.69944
28	-0.02159	0.79930
29	-0.02429	0.89915
30	-0.02662	0.99898
31	-0.02862	1.09882
32	-0.03032	1.19868
33	-0.03178	1.29856
34	-0.03301	1.39847
35	-0.03403	1.49839
36	-0.03486	1.59832
37	-0.03550	1.69826
38	-0.03594	1.79820
39	-0.03620	1.89809

Table S17. Cartesian coordinates (in Å) of the **aT–sT** transition state as optimized at the B3LYP/6-311++G(3df,3pd) level of theory.

Atom	X	Y	Z
C	0.000000	0.526379	0.000000
S	-0.478441	-1.257524	0.000000
N	-0.874387	1.378837	0.000000
H	-1.555235	2.095033	0.000000
C	1.497109	0.761759	0.000000
H	1.952410	0.307582	0.880723
H	1.952410	0.307582	-0.880723
H	1.693900	1.830980	0.000000
H	0.749627	-1.801473	0.000000

Table S18. Unscaled harmonic vibrational frequencies (E_{harm}, in cm^{-1}) and absolute IR intensities (I, in km mol^{-1}) of the **aT–sT** transition state as calculated at the B3LYP/6-311+G(d,p) level of theory.

Mode number	E_{harm}	I
1	3917.1777	426.1651
2	3132.0206	12.9326
3	3098.7171	5.4092
4	3036.0112	6.1218
5	2673.8088	2.7127
6	1824.0915	393.3831
7	1478.6402	11.8557
8	1474.7083	8.9388
9	1387.0935	12.0539
10	1108.0083	78.6323
11	1028.0540	0.1060
12	990.7994	25.1901
13	811.5325	16.4502
14	579.1038	70.3325
15	504.9365	0.1058
16	423.4183	111.9626
17	394.5879	24.3527
18	335.3085	1.3952
19	281.1091	4.5880
20	141.0180	0.0924
21	i 1059.1018	196.1595

Table S19. Relative energies (ΔE, in hartree) for the minimum-energy path along the intrinsic reaction coordinate (IRC, in bohr) originating from the **aT–sT** transition state (IRC = 0) as calculated at the B3LYP/6-311++G(3df,3pd) level of theory.

	ΔE	IRC
1	-0.03749	-1.79671
2	-0.03731	-1.69831
3	-0.03686	-1.59850
4	-0.03614	-1.49859
5	-0.03513	-1.39866
6	-0.03384	-1.29872
7	-0.03226	-1.19879
8	-0.03037	-1.09887
9	-0.02817	-0.99897
10	-0.02564	-0.89910
11	-0.02275	-0.79926
12	-0.01949	-0.69941
13	-0.01591	-0.59955
14	-0.01213	-0.49965
15	-0.00841	-0.39974
16	-0.00503	-0.29980
17	-0.00233	-0.19987
18	-0.00060	-0.09994
19	0.00000	0.00000
20	-0.00059	0.09994
21	-0.00227	0.19986
22	-0.00483	0.29980
23	-0.00799	0.39973
24	-0.01144	0.49964
25	-0.01488	0.59953
26	-0.01812	0.69940
27	-0.02104	0.79924
28	-0.02361	0.89908
29	-0.02584	0.99892
30	-0.02777	1.09878
31	-0.02945	1.19868
32	-0.03090	1.29859
33	-0.03213	1.39853
34	-0.03314	1.49848
35	-0.03395	1.59843
36	-0.03456	1.69838
37	-0.03495	1.79827
38	-0.03514	1.89762

Table S20. Cartesian coordinates (in Å) of the **aC–aT–1** transition state as optimized at the B3LYP/6-311++G(3df,3pd) level of theory.

Atom	X	Y	Z
C	-0.462740	0.186761	-0.002754
S	1.344097	-0.096880	-0.082413
N	-0.871789	1.377816	-0.000971
H	-1.893059	1.414874	0.026486
C	-1.295537	-1.065186	0.006943
H	-1.070818	-1.670823	-0.871831
H	-1.049537	-1.675024	0.877140
H	-2.359796	-0.829687	0.020106
H	1.519847	-0.063414	1.248374

Table S21. Unscaled harmonic vibrational frequencies (E_{harm}, in cm^{-1}) and absolute IR intensities (I, in km mol^{-1}) of the **aC–aT–1** transition state as calculated at the B3LYP/6-311+G(d,p) level of theory.

Mode number	E_{harm}	I
1	3417.5437	2.7100
2	3106.4106	16.8175
3	3094.3163	3.9879
4	3029.1417	9.1358
5	2677.2106	0.2730
6	1699.3629	113.0216
7	1475.8492	21.3621
8	1467.1849	12.0581
9	1406.2600	14.6614
10	1289.6114	79.1920
11	1081.7431	4.9567
12	1060.6450	50.3230
13	961.2260	33.8080
14	945.6359	46.0589
15	807.2731	8.8102
16	615.6612	35.9479
17	450.3261	2.2303
18	442.7899	4.2036
19	337.4697	1.3791
20	190.5629	0.1046
21	i 314.5118	12.2108

12

Table S22. Relative energies (ΔE, in hartree) for the minimum-energy path along the intrinsic reaction coordinate (IRC, in bohr) originating from the **aC–aT–1** transition state (IRC = 0) as calculated at the B3LYP/6-311++G(3df,3pd) level of theory.

	ΔE	IRC
1	-0.01130	-2.79872
2	-0.01124	-2.69882
3	-0.01110	-2.59887
4	-0.01089	-2.49892
5	-0.01060	-2.39896
6	-0.01026	-2.29901
7	-0.00985	-2.19905
8	-0.00939	-2.09909
9	-0.00888	-1.99913
10	-0.00833	-1.89917
11	-0.00775	-1.79921
12	-0.00714	-1.69925
13	-0.00652	-1.59929
14	-0.00589	-1.49933
15	-0.00527	-1.39937
16	-0.00464	-1.29941
17	-0.00404	-1.19945
18	-0.00346	-1.09949
19	-0.00290	-0.99954
20	-0.00238	-0.89958
21	-0.00191	-0.79962
22	-0.00147	-0.69967
23	-0.00109	-0.59971
24	-0.00076	-0.49976
25	-0.00049	-0.39981
26	-0.00028	-0.29986
27	-0.00012	-0.19991
28	-0.00003	-0.09997
29	0.00000	0.00000
30	-0.00003	0.09997
31	-0.00012	0.19991
32	-0.00027	0.29986
33	-0.00048	0.39981
34	-0.00073	0.49977
35	-0.00104	0.59972
36	-0.00139	0.69968
37	-0.00179	0.79963
38	-0.00222	0.89959
39	-0.00267	0.99955
40	-0.00315	1.09951
41	-0.00365	1.19947
42	-0.00416	1.29943
43	-0.00467	1.39939
44	-0.00518	1.49935

13

45	-0.00568	1.59931
46	-0.00617	1.69927
47	-0.00664	1.79923
48	-0.00707	1.89919
49	-0.00748	1.99914
50	-0.00786	2.09910
51	-0.00820	2.19904
52	-0.00850	2.29898
53	-0.00875	2.39891
54	-0.00897	2.49882
55	-0.00914	2.59868
56	-0.00927	2.69843
57	-0.00937	2.79799
58	-0.00945	2.89740
59	-0.00951	2.99697
60	-0.00955	3.09680
61	-0.00958	3.19675
62	-0.00960	3.29673

Table S23. Cartesian coordinates (in Å) of the **aC–aT–2** transition state as optimized at the B3LYP/6-311++G(3df,3pd) level of theory.

Atom	X	Y	Z
C	0.462740	0.186761	-0.002754
S	-1.344097	-0.096880	-0.082413
N	0.871789	1.377816	-0.000971
H	1.893059	1.414874	0.026486
C	1.295537	-1.065186	0.006943
H	1.049537	-1.675023	0.877140
H	1.070818	-1.670823	-0.871831
H	2.359796	-0.829687	0.020106
H	-1.519847	-0.063414	1.248374

Table S24. Unscaled harmonic vibrational frequencies (E_{harm}, in cm^{-1}) and absolute IR intensities (I, in km mol^{-1}) of the **aC–aT–2** transition state as calculated at the B3LYP/6-311+G(d,p) level of theory.

Mode number	E_{harm}	I
1	3417.5437	2.7100
2	3106.4114	16.8175
3	3094.3190	3.9876
4	3029.1432	9.1361
5	2677.2106	0.2730
6	1699.3629	113.0217
7	1475.8488	21.3620
8	1467.1849	12.0581
9	1406.2596	14.6615
10	1289.6114	79.1920
11	1081.7429	4.9566
12	1060.6447	50.3232
13	961.2260	33.8079
14	945.6359	46.0588
15	807.2729	8.8102
16	615.6611	35.9479
17	450.3258	2.2303
18	442.7899	4.2036
19	337.4696	1.3791
20	190.5592	0.1046
21	i 314.5118	12.2108

Table S25. Relative energies (ΔE, in hartree) for the minimum-energy path along the intrinsic reaction coordinate (IRC, in bohr) originating from the **aC–aT–2** transition state (IRC = 0) as calculated at the B3LYP/6-311++G(3df,3pd) level of theory.

	ΔE	IRC
1	-0.01130	-2.79872
2	-0.01124	-2.69882
3	-0.01110	-2.59887
4	-0.01089	-2.49892
5	-0.01060	-2.39896
6	-0.01026	-2.29901
7	-0.00985	-2.19905
8	-0.00939	-2.09909
9	-0.00888	-1.99913
10	-0.00833	-1.89917
11	-0.00775	-1.79921
12	-0.00714	-1.69925
13	-0.00652	-1.59929
14	-0.00589	-1.49933

15

15	-0.00527	-1.39937
16	-0.00464	-1.29941
17	-0.00404	-1.19945
18	-0.00346	-1.09949
19	-0.00290	-0.99954
20	-0.00238	-0.89958
21	-0.00191	-0.79962
22	-0.00147	-0.69967
23	-0.00109	-0.59971
24	-0.00076	-0.49976
25	-0.00049	-0.39981
26	-0.00028	-0.29986
27	-0.00012	-0.19991
28	-0.00003	-0.09997
29	0.00000	0.00000
30	-0.00003	0.09997
31	-0.00012	0.19991
32	-0.00027	0.29986
33	-0.00048	0.39981
34	-0.00073	0.49977
35	-0.00104	0.59972
36	-0.00139	0.69968
37	-0.00179	0.79963
38	-0.00222	0.89959
39	-0.00267	0.99955
40	-0.00315	1.09951
41	-0.00365	1.19947
42	-0.00416	1.29943
43	-0.00467	1.39939
44	-0.00518	1.49935
45	-0.00568	1.59931
46	-0.00617	1.69927
47	-0.00664	1.79923
48	-0.00707	1.89919
49	-0.00748	1.99914
50	-0.00786	2.09910
51	-0.00820	2.19904
52	-0.00850	2.29898
53	-0.00875	2.39891
54	-0.00897	2.49882
55	-0.00914	2.59868
56	-0.00927	2.69843
57	-0.00937	2.79799
58	-0.00945	2.89740
59	-0.00951	2.99697
60	-0.00955	3.09680
61	-0.00958	3.19675
62	-0.00960	3.29673

Table S26. Cartesian coordinates (in Å) of the **sC–sT–1** transition state as optimized at the B3LYP/6-311++G(3df,3pd) level of theory.

Atom	X	Y	Z
C	-0.485141	0.197122	-0.002898
S	1.325433	-0.173667	-0.082062
N	-0.941534	1.368774	0.002535
H	-0.206514	2.072046	-0.030442
C	-1.375223	-1.007065	0.010397
H	-1.179711	-1.626848	-0.865870
H	-1.162980	-1.624521	0.884239
H	-2.417779	-0.697906	0.019063
H	1.512975	-0.065859	1.243270

Table S27. Unscaled harmonic vibrational frequencies (E_{harm}, in cm^{-1}) and absolute IR intensities (I, in km mol^{-1}) of the **sC–sT–1** transition state as calculated at the B3LYP/6-311+G(d,p) level of theory.

Mode number	E_{harm}	I
1	3481.8849	8.0624
2	3132.2536	10.0013
3	3091.2503	5.1258
4	3036.3809	4.1867
5	2676.7449	0.3486
6	1714.3638	98.2039
7	1473.3079	12.6672
8	1468.1598	11.7926
9	1406.8222	12.6509
10	1271.2975	219.6149
11	1082.5516	7.7944
12	1068.8798	24.4776
13	969.4112	20.1411
14	955.3992	18.6825
15	801.9698	42.3205
16	599.5039	31.3815
17	447.7564	1.8226
18	423.9754	9.9576
19	330.6039	0.5676
20	193.3952	0.4257
21	i 254.5597	12.7224

17

Physical Chemistry Chemical Physics

Table S28. Relative energies (ΔE, in hartree) for the minimum-energy path along the intrinsic reaction coordinate (IRC, in bohr) originating from the **sC–sT–1** transition state (IRC = 0) as calculated at the B3LYP/6-311++G(3df,3pd) level of theory.

	ΔE	IRC
1	-0.00683	-2.69867
2	-0.00677	-2.59877
3	-0.00667	-2.49883
4	-0.00653	-2.39888
5	-0.00633	-2.29893
6	-0.00610	-2.19898
7	-0.00584	-2.09903
8	-0.00554	-1.99907
9	-0.00521	-1.89912
10	-0.00486	-1.79917
11	-0.00449	-1.69921
12	-0.00411	-1.59926
13	-0.00372	-1.49930
14	-0.00333	-1.39935
15	-0.00294	-1.29939
16	-0.00257	-1.19944
17	-0.00220	-1.09948
18	-0.00185	-0.99953
19	-0.00153	-0.89957
20	-0.00122	-0.79962
21	-0.00095	-0.69966
22	-0.00070	-0.59971
23	-0.00049	-0.49976
24	-0.00032	-0.39981
25	-0.00018	-0.29986
26	-0.00008	-0.19991
27	-0.00002	-0.09997
28	0.00000	0.00000
29	-0.00002	0.09997
30	-0.00008	0.19991
31	-0.00018	0.29986
32	-0.00032	0.39982
33	-0.00049	0.49977
34	-0.00070	0.59972
35	-0.00094	0.69968
36	-0.00121	0.79964
37	-0.00151	0.89960
38	-0.00183	0.99955
39	-0.00217	1.09951
40	-0.00252	1.19947
41	-0.00288	1.29943
42	-0.00324	1.39939
43	-0.00361	1.49935
44	-0.00397	1.59931

45	-0.00432	1.69927
46	-0.00466	1.79922
47	-0.00498	1.89918
48	-0.00528	1.99913
49	-0.00556	2.09908
50	-0.00582	2.19902
51	-0.00604	2.29896
52	-0.00624	2.39888
53	-0.00642	2.49878
54	-0.00656	2.59865
55	-0.00669	2.69848
56	-0.00679	2.79828
57	-0.00687	2.89805
58	-0.00694	2.99784
59	-0.00699	3.09769
60	-0.00703	3.19759
61	-0.00706	3.29754
62	-0.00707	3.39752

Table S29. Cartesian coordinates (in Å) of the **sC–sT–2** transition states as optimized at the B3LYP/6-311++G(3df,3pd) level of theory.

Atom	X	Y	Z
C	0.485141	0.197122	-0.002898
S	-1.325433	-0.173667	-0.082062
N	0.941534	1.368774	0.002535
H	0.206514	2.072046	-0.030442
C	1.375223	-1.007065	0.010397
H	1.162980	-1.624521	0.884239
H	1.179711	-1.626848	-0.865870
H	2.417779	-0.697906	0.019063
H	-1.512975	-0.065859	1.243270

19

Table S30. Unscaled harmonic vibrational frequencies (E_{harm}, in cm^{-1}) and absolute IR intensities (I, in km mol^{-1}) of the **sC–sT–2** transition state as calculated at the B3LYP/6-311+G(d,p) level of theory.

Mode number	E_{harm}	I
1	3481.8849	8.0624
2	3132.2536	10.0013
3	3091.2503	5.1258
4	3036.3809	4.1867
5	2676.7449	0.3486
6	1714.3638	98.2039
7	1473.3079	12.6672
8	1468.1598	11.7925
9	1406.8222	12.6509
10	1271.2975	219.6149
11	1082.5516	7.7944
12	1068.8798	24.4776
13	969.4112	20.1411
14	955.3992	18.6825
15	801.9698	42.3205
16	599.5039	31.3815
17	447.7564	1.8226
18	423.9754	9.9576
19	330.6039	0.5676
20	193.3952	0.4257
21	i 254.5597	12.7224

Table S31. Relative energies (ΔE, in hartree) for the minimum-energy path along the intrinsic reaction coordinate (IRC, in bohr) originating from the **sC–sT–2** transition state (IRC = 0) as calculated at the B3LYP/6-311++G(3df,3pd) level of theory.

	ΔE	IRC
1	-0.00683	-2.69867
2	-0.00677	-2.59877
3	-0.00667	-2.49883
4	-0.00653	-2.39888
5	-0.00633	-2.29893
6	-0.00610	-2.19898
7	-0.00584	-2.09903
8	-0.00554	-1.99907
9	-0.00521	-1.89912
10	-0.00486	-1.79917
11	-0.00449	-1.69921
12	-0.00411	-1.59926
13	-0.00372	-1.49930
14	-0.00333	-1.39935

15	-0.00294	-1.29939
16	-0.00257	-1.19944
17	-0.00220	-1.09948
18	-0.00185	-0.99953
19	-0.00153	-0.89957
20	-0.00122	-0.79962
21	-0.00095	-0.69966
22	-0.00070	-0.59971
23	-0.00049	-0.49976
24	-0.00032	-0.39981
25	-0.00018	-0.29986
26	-0.00008	-0.19991
27	-0.00002	-0.09997
28	0.00000	0.00000
29	-0.00002	0.09997
30	-0.00008	0.19991
31	-0.00018	0.29986
32	-0.00032	0.39982
33	-0.00049	0.49977
34	-0.00070	0.59972
35	-0.00094	0.69968
36	-0.00121	0.79964
37	-0.00151	0.89960
38	-0.00183	0.99955
39	-0.00217	1.09951
40	-0.00252	1.19947
41	-0.00288	1.29943
42	-0.00324	1.39939
43	-0.00361	1.49935
44	-0.00397	1.59931
45	-0.00432	1.69927
46	-0.00466	1.79922
47	-0.00498	1.89918
48	-0.00528	1.99913
49	-0.00556	2.09908
50	-0.00582	2.19902
51	-0.00604	2.29896
52	-0.00624	2.39888
53	-0.00642	2.49878
54	-0.00656	2.59865
55	-0.00669	2.69848
56	-0.00679	2.79828
57	-0.00687	2.89805
58	-0.00694	2.99784
59	-0.00699	3.09769
60	-0.00703	3.19759
61	-0.00706	3.29754
62	-0.00707	3.39752

21

Table S32. Cartesian coordinates (in Å) of the **Tn** tautomer as optimized by the CBS-QB3 method.

Atom	X	Y	Z
C	-0.277532	-0.060914	0.000000
S	1.370023	0.119162	0.000000
N	-0.872014	-1.269617	0.000000
H	-0.298082	-2.098419	0.000000
H	-1.874853	-1.372436	0.000000
C	-1.239175	1.105289	0.000000
H	-1.883474	1.065535	0.884940
H	-0.694315	2.044495	0.000000
H	-1.883474	1.065535	-0.884940

Table S33. Cartesian coordinates (in Å) of the **aC** isomer as optimized by the CBS-QB3 method.

Atom	X	Y	Z
C	0.000000	0.483375	0.000000
S	-0.335705	-1.282054	0.000000
N	-0.967297	1.299720	0.000000
H	-0.624559	2.262682	0.000000
C	1.478816	0.795602	0.000000
H	1.963392	0.367560	0.881777
H	1.963392	0.367560	-0.881777
H	1.637922	1.875413	0.000000
H	-1.670680	-1.132257	0.000000

Table S34. Cartesian coordinates (in Å) of the **aT** isomer as optimized by the CBS-QB3 method.

Atom	X	Y	Z
C	0.000000	0.486527	0.000000
S	-0.498333	-1.240743	0.000000
N	-0.949868	1.322251	0.000000
H	-0.593023	2.278935	0.000000
C	1.483583	0.773315	0.000000
H	1.961966	0.341596	0.883197
H	1.961966	0.341596	-0.883197
H	1.656830	1.851640	0.000000
H	0.733157	-1.776689	0.000000

Table S35. Cartesian coordinates (in Å) of the **sC** isomer as optimized by the CBS-QB3 method.

Atom	X	Y	Z
C	0.000000	0.507464	0.000000
S	-0.302955	-1.284087	0.000000
N	-0.864041	1.429016	0.000000
H	-1.823519	1.083678	0.000000
C	1.473915	0.821169	0.000000
H	1.960312	0.397230	0.882823
H	1.960312	0.397230	-0.882823
H	1.599383	1.902762	0.000000
H	-1.644411	-1.210424	0.000000

Table S36. Cartesian coordinates (in Å) of the **sT** isomer as optimized by the CBS-QB3 method.

Atom	X	Y	Z
C	0.000000	0.506587	0.000000
S	-0.449644	-1.250654	0.000000
N	-0.871071	1.422248	0.000000
H	-1.828002	1.065912	0.000000
C	1.470395	0.829694	0.000000
H	1.960184	0.412154	0.883943
H	1.960184	0.412154	-0.883943
H	1.586484	1.912879	0.000000
H	0.790576	-1.766051	0.000000

Table S37. Cartesian coordinates (in Å) of the **Tn–aC** transition state as optimized by the CBS-QB3 method.

Atom	X	Y	Z
C	0.000000	0.404923	0.000000
S	-0.019184	-1.332313	0.000000
N	-1.238284	0.798980	0.000000
H	-1.490915	-0.574639	0.000000
H	-1.463923	1.794322	0.000000
C	1.218737	1.272575	0.000000
H	1.829284	1.053449	0.878925
H	1.829284	1.053449	-0.878925
H	0.958785	2.332578	0.000000

Table S38. Cartesian coordinates (in Å) of the **aC–sC** transition state as optimized by the CBS-QB3 method.

Atom	X	Y	Z
C	0.000000	0.541427	0.000000
S	-0.321659	-1.313520	0.000000
N	-0.887339	1.377355	0.000000
H	-1.578234	2.085424	0.000000
C	1.498224	0.784742	0.000000
H	1.693068	1.856762	0.000000
H	1.955090	0.328096	0.882190
H	1.955090	0.328096	-0.882190
H	-1.656440	-1.180561	0.000000

Table S39. Cartesian coordinates (in Å) of the **aT–sT** transition state as optimized by the CBS-QB3 method.

Atom	X	Y	Z
C	0.000000	0.537329	0.000000
S	-0.475570	-1.270127	0.000000
N	-0.883058	1.379514	0.000000
H	-1.566681	2.094586	0.000000
C	1.499728	0.777381	0.000000
H	1.958607	0.325610	0.883343
H	1.958607	0.325610	-0.883343
H	1.689698	1.850793	0.000000
H	0.751931	-1.819423	0.000000

Table S40. Cartesian coordinates (in Å) of the **aC–aT–1** transition state as optimized by the CBS-QB3 method.

Atom	X	Y	Z
C	-0.468378	0.189811	-0.002012
S	1.348572	-0.098188	-0.082500
N	-0.872073	1.384431	-0.001167
H	-1.896733	1.411381	0.026264
C	-1.298973	-1.068842	0.006712
H	-1.072067	-1.675655	-0.873868
H	-1.055000	-1.680118	0.879804
H	-2.367199	-0.836418	0.017822
H	1.522469	-0.065011	1.249940

Table S41. Cartesian coordinates (in Å) of the **aC–aT–2** transition state as optimized by the CBS-QB3 method.

Atom	X	Y	Z
C	0.468378	0.189811	-0.002012
S	-1.348572	-0.098188	-0.082500
N	0.872073	1.384431	-0.001167
H	1.896733	1.411381	0.026264
C	1.298973	-1.068842	0.006712
H	1.055000	-1.680118	0.879803
H	1.072068	-1.675655	-0.873869
H	2.367199	-0.836419	0.017823
H	-1.522469	-0.065011	1.249940

Table S42. Cartesian coordinates (in Å) of the **sC–sT–1** transition state as optimized by the CBS-QB3 method.

Atom	X	Y	Z
C	-0.489970	0.198587	-0.002294
S	1.332517	-0.176179	-0.081667
N	-0.947908	1.370907	0.000240
H	-0.205007	2.069405	-0.037837
C	-1.380465	-1.010179	0.012235
H	-1.184045	-1.634381	-0.863880
H	-1.175072	-1.625989	0.892040
H	-2.423829	-0.694167	0.015137
H	1.525644	-0.022800	1.239887

Table S43. Cartesian coordinates (in Å) of the **sC–sT–2** transition state as optimized by the CBS-QB3 method.

Atom	X	Y	Z
C	0.489970	0.198587	-0.002294
S	-1.332517	-0.176179	-0.081667
N	0.947908	1.370907	0.000240
H	0.205007	2.069405	-0.037837
C	1.380465	-1.010179	0.012235
H	1.175071	-1.625989	0.892040
H	1.184045	-1.634381	-0.863880
H	2.423829	-0.694167	0.015137
H	-1.525644	-0.022799	1.239887

25

Table S44. Relative zero-point corrected energies (ΔE_{ZPE})[a] of the thioacetamide isomers (minima) and the first-order transition states (TSs) computed by the CBS-QB3 method, as well as conformationally-relevant dihedral angles (φ_1 and φ_2).[b]

Structures	φ_1	φ_2	ΔE_{ZPE}	$\Delta\Delta E^{\#}(\rightarrow)$	$\Delta\Delta E^{\#}(\leftarrow)$
minima					
Tn	–	–	−37.6	–	–
aC	180.0	0.0	1.7	–	–
aT	180.0	180.0	6.1	–	–
sC	0.0	0.0	1.1	–	–
sT	0.0	180.0	0.0	–	–
TSs					
Tn–aC	180.0	0.0	111.1	148.8	109.4
aC–sC	180.0	0.0	98.6	96.9	97.5
aT–sT	180.0	−180.0	100.2	94.2	100.2
aC–aT–1	178.8	88.7	27.3	25.6	21.2
aC–aT–2	−178.8	−88.7	27.3	25.6	21.2
sC–sT–1	−0.5	83.3	15.7	14.6	15.7
sC–sT–2	0.5	−83.3	15.7	14.6	15.7

[a] All energies in kJ mol^{-1}, the energy of isomer **sT** was chosen as the relative zero.

[b] In degrees, φ_1 = H–N=C–S, φ_2 = H–S–C=N, see also Figure 1.

Table S45. Cartesian coordinates (in Å) of the **Tn** tautomer as optimized by the G4 method.

Atom	X	Y	Z
C	0.000000	0.284491	0.000000
S	-0.170425	-1.361902	0.000000
N	-1.056858	1.117483	0.000000
H	-1.987275	0.731314	0.000000
H	-0.948017	2.118744	0.000000
C	1.340122	0.984014	0.000000
H	1.435928	1.625629	0.884316
H	2.147511	0.255699	0.000000
H	1.435928	1.625629	-0.884316

Table S46. Cartesian coordinates (in Å) of the **aC** isomer as optimized by the G4 method.

Atom	X	Y	Z
C	0.000000	0.480764	0.000000
S	-0.339336	-1.277191	0.000000
N	-0.962649	1.305814	0.000000
H	-0.609061	2.265340	0.000000
C	1.479975	0.784788	0.000000
H	1.964454	0.352804	0.881761
H	1.964454	0.352804	-0.881761
H	1.645785	1.864848	0.000000
H	-1.677565	-1.134746	0.000000

Table S47. Cartesian coordinates (in Å) of the **aT** isomer as optimized by the G4 method.

Atom	X	Y	Z
C	0.000000	0.484742	0.000000
S	-0.505229	-1.235283	0.000000
N	-0.940844	1.333673	0.000000
H	-0.568638	2.284991	0.000000
C	1.485716	0.756307	0.000000
H	1.961858	0.317942	0.883104
H	1.961858	0.317942	-0.883104
H	1.671814	1.833805	0.000000
H	0.728384	-1.772156	0.000000

Table S48. Cartesian coordinates (in Å) of the **sC** isomer as optimized by the G4 method.

Atom	X	Y	Z
C	0.000000	0.504965	0.000000
S	-0.305771	-1.278389	0.000000
N	-0.860554	1.432427	0.000000
H	-1.822118	1.092128	0.000000
C	1.475851	0.810373	0.000000
H	1.960235	0.380268	0.882649
H	1.960235	0.380268	-0.882649
H	1.612792	1.892051	0.000000
H	-1.650045	-1.209502	0.000000

27

Table S49. Cartesian coordinates (in Å) of the **sT** isomer as optimized by the G4 method.

Atom	X	Y	Z
C	0.000000	0.504520	0.000000
S	-0.451613	-1.244590	0.000000
N	-0.869283	1.424776	0.000000
H	-1.827168	1.070059	0.000000
C	1.471777	0.819507	0.000000
H	1.959618	0.395465	0.883697
H	1.959618	0.395465	-0.883697
H	1.600070	1.902860	0.000000
H	0.787983	-1.768014	0.000000

Table S50. Cartesian coordinates (in Å) of the **Tn–aC** transition state as optimized by the G4 method.

Atom	X	Y	Z
C	0.000000	0.403298	0.000000
S	-0.015309	-1.330644	0.000000
N	-1.241004	0.791698	0.000000
H	-1.480505	-0.578951	0.000000
H	-1.469696	1.785971	0.000000
C	1.213424	1.276917	0.000000
H	1.827135	1.061645	0.879520
H	1.827135	1.061645	-0.879520
H	0.947355	2.336828	0.000000

Table S51. Cartesian coordinates (in Å) of the **aC–sC** transition state as optimized by the G4 method.

Atom	X	Y	Z
C	0.000000	0.540205	0.000000
S	-0.327101	-1.306229	0.000000
N	-0.880198	1.382048	0.000000
H	-1.562947	2.094103	0.000000
C	1.500837	0.769823	0.000000
H	1.710384	1.840457	0.000000
H	1.953879	0.306095	0.882154
H	1.953879	0.306095	-0.882154
H	-1.665218	-1.181591	0.000000

Table S52. Cartesian coordinates (in Å) of the **aT–sT** transition state as optimized by the G4 method.

Atom	X	Y	Z
C	0.000000	0.537161	0.000000
S	-0.484106	-1.263544	0.000000
N	-0.871650	1.389267	0.000000
H	-1.543565	2.111540	0.000000
C	1.503217	0.757727	0.000000
H	1.956895	0.297265	0.883300
H	1.956895	0.297265	-0.883300
H	1.711997	1.829095	0.000000
H	0.745716	-1.812650	0.000000

Table S53. Cartesian coordinates (in Å) of the **aC–aT–1** transition state as optimized by the G4 method.

Atom	X	Y	Z
C	-0.464627	0.188443	-0.003571
S	1.345778	-0.098237	-0.082553
N	-0.870939	1.384485	-0.000992
H	-1.895864	1.410645	0.028137
C	-1.297448	-1.067714	0.007142
H	-1.074417	-1.676792	-0.874817
H	-1.051236	-1.681525	0.879783
H	-2.366313	-0.832978	0.021979
H	1.524409	-0.063330	1.251279

Table S54. Cartesian coordinates (in Å) of the **aC–aT–2** transition state as optimized by the G4 method.

Atom	X	Y	Z
C	0.464627	0.188443	-0.003571
S	-1.345778	-0.098237	-0.082553
N	0.870939	1.384485	-0.000992
H	1.895864	1.410645	0.028137
C	1.297448	-1.067714	0.007142
H	1.051235	-1.681525	0.879782
H	1.074417	-1.676792	-0.874818
H	2.366313	-0.832978	0.021980
H	-1.524409	-0.063330	1.251279

29

Table S55. Cartesian coordinates (in Å) of the **sC–sT–1** transition state as optimized by the G4 method.

Atom	X	Y	Z
C	-0.486954	0.198362	-0.003709
S	1.328981	-0.172686	-0.082164
N	-0.948537	1.371346	0.002686
H	-0.207635	2.072605	-0.032191
C	-1.375236	-1.012013	0.010835
H	-1.180203	-1.633658	-0.869136
H	-1.160597	-1.632380	0.887055
H	-2.422136	-0.702919	0.021688
H	1.519779	-0.058191	1.245647

Table S56. Cartesian coordinates (in Å) of the **sC–sT–2** transition state as optimized by the G4 method.

Atom	X	Y	Z
C	0.486954	0.198362	-0.003709
S	-1.328981	-0.172686	-0.082164
N	0.948537	1.371346	0.002686
H	0.207635	2.072605	-0.032191
C	1.375236	-1.012013	0.010835
H	1.160597	-1.632380	0.887055
H	1.180203	-1.633658	-0.869136
H	2.422136	-0.702919	0.021688
H	-1.519779	-0.058191	1.245647

30

Table S57. Relative zero-point corrected energies (ΔE_{ZPE})[a] of the thioacetamide isomers (minima) and the first-order transition states (TSs) computed by the G4 method, as well as conformationally-relevant dihedral angles (φ_1 and φ_2).[b]

Structures	φ_1	φ_2	ΔE_{ZPE}	$\Delta\Delta E^{\#}(\rightarrow)$	$\Delta\Delta E^{\#}(\leftarrow)$
minima					
Tn	–	–	−36.6	–	–
aC	180.0	0.0	1.3	–	–
aT	180.0	180.0	5.9	–	–
sC	0.0	0.0	1.0	–	–
sT	0.0	180.0	0.0	–	–
TSs					
Tn–aC	180.0	0.0	111.7	148.2	110.4
aC–sC	180.0	0.0	101.5	100.2	100.5
aT–sT	180.0	−180.0	103.1	97.2	103.1
aC–aT–1	179.0	88.5	27.1	25.9	21.2
aC–aT–2	−179.0	−88.5	27.1	25.9	21.2
sC–sT–1	−0.5	84.8	15.7	14.7	15.7
sC–sT–2	0.5	−84.8	15.7	14.7	15.7

[a] All energies in kJ mol^{-1}, the energy of isomer **sT** was chosen as the relative zero.

[b] In degrees, φ_1 = H–N=C–S, φ_2 = H–S–C=N, see also Figure 1.